Flexible rotor blade dynamics for helicopter aeromechanics including comparisons with experimental data

I. Goulos
i.goulos@cranfield.ac.uk
V. Pachidis and P. Pilidis
School of Aerospace, Transport and Manufacturing
Cranfield University
Bedford
UK

ABSTRACT

This paper presents the development of a mathematical model for the implementation of flexible rotor blade dynamics in real-time helicopter aeromechanics applications. A Lagrangian approach is formulated for the rapid estimation of natural vibration characteristics of nonuniform rotor blades. A matrix/vector formulation is proposed for the treatment of elastic blade kinematics in the time-domain. In order to overcome the classical hurdles of time-accurate simulation and establish applicability in real-time, a novel, second-order accurate, finite-difference scheme is employed for the numerical discretisation of elastic blade motion. The proposed rotor dynamics model is coupled with a finite-state induced flow and an unsteady blade element aerodynamics model. The combined formulation is implemented in a helicopter flight mechanics simulation code. The integrated approach is deployed in order to investigate rotor blade resonant frequencies, trim control angles, oscillatory blade loads and induced vibration for a hingeless and an articulated helicopter rotor. Extensive comparisons are carried out with wind tunnel and flight test measurements, and non-real-time comprehensive analysis methods. Good agreement with measured data is exhibited considering primarily the low-frequency harmonic components of oscillatory loading. It is shown that, the developed methodology can be utilised for real-time simulation on a typical computer with sufficient modelling fidelity for accurate estimation of oscillatory blade loads.

Paper No. 4025. Manuscript received 1 July 2013, revised version received 1 November 2013, second revision received 30 June 2014, accepted 16 July 2014.

https://doi.org/10.1017/S0001924000010496 Published online by Cambridge University Press

NOMENCLATURE

$A(r)$, $I(r)$	cross-sectional area and area moment of inertia, m^2, m^4
A, B, C, D	mode shape equation integration constants used in classical methods
A_i	rotating reference frame of the ith blade index, $i = 1, \ldots N_b$
$\mathbf{A}^{flap/lag/torsion}_{Lagrange}$	Lagrange's equation coefficient matrix
$\mathbf{A_i}$	global O to rotating reference frame A_i transformation matrix, $i = 1, \ldots N_b$
b	blade element local co-ordinate system index
C_t, C_L, C_M	rotor thrust, rolling and pitching moment coefficients
$\mathrm{d}\mathbf{f}^O_p$, $\mathrm{d}\mathbf{m}^O_p$	beam element total differential force and moment loads vectors, N, Nm
e	blade root/hinge offset distance from the centre of rotation as a fraction of rotor blade radius
E, G	material Young's/stress modulus, Pa
$\mathbf{e}_\mathbf{x}^{\mathbf{A_i}}$, $\mathbf{e}_\mathbf{y}^{\mathbf{A_i}}$, $\mathbf{e}_\mathbf{z}^{\mathbf{A_i}}$	rotating blade reference frame A_i unit vectors
$\mathbf{e}_\mathbf{x}^\mathbf{b}$, $\mathbf{e}_\mathbf{y}^\mathbf{b}$, $\mathbf{e}_\mathbf{z}^\mathbf{b}$	local blade element co-ordinate system b unit vectors
$\mathbf{e}_\mathbf{x}$, $\mathbf{e}_\mathbf{y}$, $\mathbf{e}_\mathbf{z}$	global non-rotating reference frame O unit vectors
$\mathbf{f}^b_{aero}$, $\mathbf{m}^b_{aero}$	aerodynamic force and moment per unit length vectors, N/m, N
$\mathbf{F}^O_i(t)$, $\mathbf{T}^O_i(t)$	force and moment vectors of the ith blade, $i = 1, \ldots N_b$, N, Nm
$\mathbf{F}^O_{rotor}(t)$, $\mathbf{T}^O_{rotor}(t)$	main rotor force and moment vectors, N, Nm
$I_p(r)$, $J(r)$	cross-sectional polar moment of inertia and torsion constant, m^2, m^4
$K^{flap/lag/torsion}$	blade hinge/pitch control system spring stiffness, N/m, rad
$m_{i,j}$, $k_{i,j}$, $f_{i,j}$, $I_{i,j}$	inter-modal coupling coefficients between the ith and jth assumed modes
N	number of mode shapes
N_b, N_{rev}	number of blades, number of rotor revolutions
O	global non-rotating reference frame index
P	per revolution
$p(r,t)$	beam element of mass $dm = \rho A(r)dr$, located at beam radius r at time t
$Q_i^{flap/lag/torsion}$	generalised centrifugal force/moment of the ith co-ordinate, $i = 1 \ldots N$
$q_i^{flap/lag/torsion}(t)$	time-dependent generalised co-ordinate of the ith mode shape, $i = 1 \ldots N$
$\bar{\mathbf{q}}_i^{flap/lag/torsion}$	ith eigenvector of Lagrange's equation matrix , $i = 1 \ldots N$
R	rotor blade radius, m
R_{comp}	computational time ratio, $= \dfrac{T_{req}}{T_{sim}}$, dimensionless
r	local beam element radius, m
$\mathbf{r}^{A_i}_{p/A_i}$	position vector of beam element $p(r,t)$ relative to the origin of A_i, m
$\mathbf{r}^{b,offset}_p$	aerofoil centre of mass offset vector from the blade elastic axis, m
$\mathbf{r}^O_{p/O}$	position vector of beam element $p(r,t)$ relative to the origin of O, m
$\mathbf{r}_{Ai/O}$	position vector of the origin of A_i, m
t	time, sec
$T^{flap/lag/torsion}$	kinetic energy of the rotor blade, Joules
T_{req}, T_{sim}	required computational time and simulated time of rotor operation, sec
$\mathbf{T}^O_{i_{offset}}(t)$	moment vector of the ith blade due to root/hinge offset, $i = 1 \ldots N_b$, Nm
$\mathbf{T}^O_{i,root}(t)$	moment vector of the ith blade due to root/hinge stiffness, $i = 1 \ldots N_b$, Nm
$\mathbf{T}^b_i$	global O to local blade element co-ordinate system b transformation matrix
$U^{flap/lag/torsion}$	strain energy of the rotor blade, Joules
$\mathbf{u}^{A_i}_{p/A_i}$, $\mathbf{a}^{A_i}_{p/A_i}$	linear velocity and acceleration vectors of beam element $p(r,t)$ relative to the origin of A_i, ms^{-1}, ms^{-2}

https://doi.org/10.1017/S0001924000010496 Published online by Cambridge University Press

$\mathbf{u}_p^O$, $\mathbf{u}_p^b$, $\mathbf{a}_p^O$, $\mathbf{a}_p^b$ absolute linear velocity and acceleration vectors of $p(r,t)$, ms^{-1}, ms^{-2}
$\mathbf{u}_o$ translational velocity vector of the global O frame, $[u_o, v_o, w_o]^T$ ms^{-1},
$\mathbf{u}_{A_i}$, $\mathbf{a}_{A_i}$ absolute linear velocity and acceleration vectors of the origin of A_i, ms^{-1}, ms^{-2}
V free-stream velocity, m/sec
$w^{flap/lag}(r,t)$ time-dependent transverse displacement, m
x effective modal co-ordinate, $= r - eR$, m
$X_i^{flap/lag/torsion}(r)$ shape for the ith mode of motion, $i = 1, \ldots N$, m (rad for torsion)
$Y_{offset}(r)$ aerofoil centre of mass offset from elastic axis, m

Greek symbols

α rotor shaft angle relative to the free-stream flow, deg
$\beta(r,t)$, $\zeta(r,t)$ local beam element equivalent flap/lag angles, $= \text{Arcsin}\dfrac{w^{flap/lag}(r,t)}{r-eR}$ rad
$\hat{\beta}$, $\hat{\zeta}$ equivalent flap and lag angles at the rotor blade hub, rad
β, ζ, $\theta_{torsion}$ local flap, lag and torsion angle rotation matrices rad
$\mathbf{B}_{pre}$, $\mathbf{Z}_{pre}$ rotor blade pre-cone and pre-sweep rotation matrices
Δt employed time-step during the time marching procedure, s
$\mathbf{\Theta}_0$, $\mathbf{\Psi}_i$ rotor blade collective pitch and azimuth angle rotation matrices
$\theta(r,t)$ time-dependent torsional deformation angle, rad
θ_0, θ_{1c}, θ_{1s} collective, lateral cyclic and longitudinal cyclic pitch angles, rad
$\theta_c(eR,t)$ cyclic pitch angle at the blade hub, rad
$\boldsymbol{\lambda}$, $\boldsymbol{\theta}_c$, $\boldsymbol{\theta}_{tw}$ local sweep, cyclic pitch and pre-twist angle rotation matrices

μ advance ratio, $= \dfrac{V}{\Omega R}$

ρ material density, kg/m^3
σ rotor solidity
$\phi_i^{flap/lag/torsion}(r)$ assumed function of the ith mode shape, $i = 1, \ldots N$, m (rad for torsion)
$\mathbf{\Phi}_i^{flap/lag/torsion}(r)$ assumed mode shape vector, $[\phi_j^{flap/lag/torsion}(r), j = 1, \ldots N]^T$
$\psi_i(t)$ azimuth angle of the ith blade root/hinge at time t, $i = 1, \ldots N_b$, rad
Ω nominal rotorspeed, rad/sec
$\omega_i^{flap/lag/torsion}$ natural vibration frequency of the ith mode of motion, $i = 1, \ldots N$, rad/sec
$\boldsymbol{\omega}_{\mathbf{p/A_i}}^{\mathbf{A_i}}$, $\dot{\boldsymbol{\omega}}_{\mathbf{p/A_i}}^{\mathbf{A_i}}$ angular velocity and acceleration vectors of beam element $p(r,t)$ relative to the origin of A_i, rad/sec, rad/sec^2
$\boldsymbol{\omega}_{\mathbf{0}}$ angular velocity vector of the global O frame, $= [p_o, q_o, r_o]^T$ rad/sec
$\boldsymbol{\omega}_{\mathbf{A_i}}$, $\dot{\boldsymbol{\omega}}_{\mathbf{A_i}}$ absolute angular velocity and acceleration vectors of the origin of A_i, rad/sec, rad/sec^2

Superscripts

$(\,)^O$ $(\,)^{A_i}$ $(\,)^b$ vector expressed in the annotated reference axes system
$(\dot{\,})(\ddot{\,})$ first and second derivatives with respect to time t
$()'()''$ first and second derivatives with respect to beam radius r
$(\,)^{flap/lag/torsion}$ referring to the flap/lag/torsion degree of freedom respectively

Subscripts

$(\,)_{A_i/}$ vector referring to the origin of the rotating reference frame of the ith blade
$(\,)_{p/}$ vector referring to beam element point $p(r,t)$

https://doi.org/10.1017/S0001924000010496 Published online by Cambridge University Press

$(\,)_{/O}(\,)_{/A_i}$	vector relative to the origin of the annotated reference axes system
$(\,)_{i,j}$	blade or mode number indices

Acronyms

BVI	blade vortex interaction
DOF	degree of freedom
F-L-T	flap-lag-torsion
FEA	finite element analysis
P	times per rotor revolution
PDE	partial differential equation

1.0 INTRODUCTION

1.1 Background

Helicopter aeromechanics is one of the most analytically complex aspects of aeronautical engineering. This complexity arises predominantly due to the multidisciplinary nature of the problem. It encompasses individual scientific disciplines related to aerodynamics, structures, rotor dynamics, and flight mechanics. In an effort to capture the multidisciplinary facet of the word 'Aeromechanics' as applied to rotorcraft, Johnson[1,2] proposed the following definition: 'Aeromechanics: The branch of aeronautical engineering and science dealing with equilibrium, motion, and control of elastic rotorcraft in air''. This definition covers key performance attributes encountered during rotorcraft design which include; loads, vibration, stability, flight dynamics, and noise. A thorough historical perspective covering milestones in rotorcraft aeromechanics is provided in Ref. 2.

The primary scope of aeromechanics as applied to helicopters lies with regards to analysing the aeroelastic behaviour of the main rotor. The main rotor holds multiple roles in the context of helicopter performance, them comprising; lift, propulsion, and control. The rotor's constant operation within a highly unsteady aerodynamic environment during forward and manoeuvring flight, essentially leads to highly unsteady exerted rotor hub loads. Obtaining accurate estimates of the unsteady forces and moments imposed by the elastic rotor blades on the aircraft fuselage, is an important requirement for rotorcraft flight mechanics. This is imperative considering investigations which include the effects of higher frequency rotor dynamics on flying and handling qualities.

Padfield[3] discussed a three-level hierarchical classification of helicopter simulation models as a means of gauging the progress of attained simulation fidelity. At the first level of modelling, a disc-like representation of the main rotor is employed using first-order dynamic inflow and linear aerodynamics. A Level 2 modelling approach may incorporate individual-blade representation coupled with a more refined induced flow model. Look-up tables are utilised in order to estimate the steady, nonlinear aerodynamic blade element response. At Level 3, the complete aeroelastic behaviour of the main rotor is simulated. This necessitates employment of a detailed structural representation of the elastic blades (modal or finite element approach) coupled with unsteady/nonlinear blade element aerodynamics and three-dimensional rotor wake induced flow modelling (free or prescribed).

Level 1-2 models are mainly deployed for the analysis of parametric trends considering flying qualities and flight performance within the limits of the operational envelope. Level 3 models are utilised for rotor design applications such as nolinear trim analysis, prediction of oscillatory structural blade loads, and rotor induced vibration up to the limits defined by the safe flight envelope.

https://doi.org/10.1017/S0001924000010496 Published online by Cambridge University Press

1.2 Aeromechanics for helicopter flight dynamics

In order to include the effects of higher frequency rotor dynamics in flight mechanics, it was necessary for the helicopter community to depart from the Level 1 disc-like representation of the main rotor and adapt methodologies that involved individual blade modelling (Levels 2 and 3). This turnaround in rotor dynamics enabled the implementation of more sophisticated rotor induced flow and blade aerodynamics models. Initial attempts at individual—blade rotor modelling treated each blade as a rigid body. Hub springs and effective hinge offsets were assumed in order to simulate the actual root stiffness of hingeless blades. An example of that particular approach is the well-known 'Genhel' rotor model, developed by Howlett in Ref. 4 for the UH-60 Blackhawk helicopter.

Considering the case of a hingeless rotor, modelling the blade as a rigid body may be viewed as an approximation to the motion of the first elastic cantilever flap and lag modes. An actual rotor blade may respond to external forcing by deforming within all of its vibration modes. The magnitude of contribution of higher-order modal content to the rotating hub forces and moments is directly related to the nature of external forcing. Shupe[5], and Curtiss and Shupe[6] investigated the effect of the second cantilever flap bending mode of a hingeless blade on the transmitted hub moment. He observed that, the higher the radial nonlinearity in the once-per-rev (1P) harmonic forcing, the greater the contribution of higher-order modal content. Hence, he concluded that including the influence of higher modes is essential for the correct prediction of hingeless rotor hub moments.

Recent advances in rotary-wing aerodynamics include the development of more refined rotor inflow[7] and blade aerodynamics models[8]. This has inevitably led to the requirement for more sophisticated rotor dynamics models in order to maintain consistent levels in the fidelity of simulation. Brown and Houston[9] carried out a comparative evaluation between a first-order finite-state dynamic inflow model[10,11] and a highly refined induced flow approach that was based on the solution of the vorticity transport equations[7]. Both inflow models were numerically coupled with a rigid-blade rotor dynamics and a fuselage kinematics model.

The capability of the aforementioned inflow theories was evaluated in terms of the predictive qualities they exhibited with respect to trim control angles, linearised stability and control derivatives, nonlinear control response and airframe vibration characteristics for the Aerospatiale SA330 helicopter. Brown *et al* noted that, an improvement in the overall level of simulation fidelity requires an integrated 'jump' in modelling complexity considering both rotor dynamics and aerodynamics. It was therefore concluded that, the classical rigid blade model would have to be abandoned if rotor dynamics models were to keep up with the fidelity of modern aerodynamic theories.

Theodore and Celi[12] developed a high-fidelity non-real-time simulation framework for helicopter flight dynamics. The baseline flight mechanics model from Ref. 13 was numerically coupled with the flexible blade model of Ref. 14 and a relaxation-type free-wake model[15]. Theodore and Celi deployed their integrated fremework in order to examine the effects of inflow and blade dynamics modelling fidelity on the accuracy of the predicted free-flight response of the Bo105 helicopter. They concluded that, neither free-wake nor flexible blade models are required for accurate prediction of the on-axis rotor response. However, they noted that accurate prediction of the off-axis rotor response cannot be accomplished without both free-wake and flexible blade modelling.

Other notable work where the effect of blade flexibility on rotor response characteristics has been examined in the context of flight dynamics includes that of Turnour and Celi[14], Lewis[16] and Sturisky and Schrage[17].

https://doi.org/10.1017/S0001924000010496 Published online by Cambridge University Press

1.3 Aeromechanics for helicopter rotor design — comprehensive analysis

Comprehensive rotorcraft codes are built predominantly for rotor design. This essentially requires reasonably accurate estimates of oscillatory structural blade loads and induced vibration[18]. High vibration conditions are typically encountered by modern rotorcraft within two specific operating regimes; transition from hover and high-speed flight. Rotor induced vibration corresponding to the former flight condition originates from impulsive blade airloads due to strong blade vortex interaction (BVI). Vibrations during high-speed flight are due to dynamic stall in the retreating side and shock-induced separation combined with negative tip loading in the advancing side.

Piziali and DuWaldt[19-23] were among the first analysts to tackle the solution of the aeroelastic response of helicopter rotor blades. Their work was partially motivated by flight test data suggesting high oscillatory structural blade loads, which were later attributed to highly nonuniform wake induced velocities. It was postulated in Ref. 23 that, the main difficulty in designing a helicopter rotor system essentially constitutes adequate estimation of performance, blade stresses and pitch control angles for given thrust/hub moment settings within steady-state flight conditions. The overall problem of rotor design was therefore elaborately broken down within three closely inter-dependent major steps of analysis; (a) prediction of aerodynamic loads, (b) dynamic response of rotor blades to external forcing, and (c) aeroelastic rotor-aircraft trim.

More recently, Yeo and Johnson[18,24,25] performed an investigation of airloads and structural blade loads for five helicopter rotors operating at transition from hover and high-speed flight conditions. They carried out extensive comparisons between predictions made with CAMRAD II (Comprehensive Analytical Model of Rotorcraft Aerodynamics and Dynamics)[26] and experimental data from wind tunnel and flight test measurements. CAMRAD II is a comprehensive rotorcraft aeromechanics analysis code that combines a series of advanced technologies including; unsteady nonlinear aerodynamics[8], free-wake modelling[27], multi-body dynamics and, finite element analysis (FEA)[28]. Yeo and Johnson [25] reported satisfactory agreement between predictions and measurements considering flap bending and torsional moments for the majority of the rotor models they investigated. Chordwise bending moment correlations were considered to be poor which was attributed to unsatisfactory predictions of chordwise airloads and lag damper modelling.

The majority of comprehensive rotorcraft codes incorporate free-wake modelling in order to predict the rotor wake induced flow. These models essentially account for the wake's self-induced distortion using a discretised three-dimensional representation of the vortical wake. Therefore, they cater for a detailed level of flow-physics and they are applicable to the prediction of BVI-related airlods. However, they are also prone to discretisation errors and real-time execution is hindered by the associated computational cost. Finite-state inflow models[29,30] have also emerged within the last couple of decades as a compromise between simulation fidelity and computational overhead. These models employ a continuous wake representation with no associated discretisation errors. The rotor wake is modelled as a skewed cylinder with no wake-roll up. The induced flow at the rotor disc is expressed as a function of a finite number of flow-states, determined by the solution of a first-order ordinary matrix differential equation. Hence, owing to their simplicity, they effectively lend themselves to real-time execution. However, they are not applicable to the prediction of BVI and their accuracy is dependent on the employed number of flow-states.

Van der Wall *et al*[31] attempted to systematically assess the potential of the modern state-of-the-art in comprehensive analysis. The capabilities of a series of current comprehensive rotorcraft codes, utilising both free-wake as well as finite-state inflow models, was evaluated and compared with experimental data derived from the HART II test (Higher harmonic control Aeroacoustics Rotor Test[32]). The HART II experiment was conducted using a 40 % geometrically and dynamically scaled-down model of the Bo105 helicopter rotor in the open-jet test section of the German-Dutch

https://doi.org/10.1017/S0001924000010496 Published online by Cambridge University Press

wind tunnel. Measurements were conducted for unsteady blade motion, section airloads, leading edge pressure distributions, tip vortex positions, tip vortex flow fields, and acoustic radiation.

Van der Wall *et al*[31]elaborated extensively on the applicability and physical accuracy of finite-state inflow models relative to that of modern free-wake aerodynamics. They arrived at the conclusion that, finite-state formulations are capable of providing estimates of aeroelastic rotor trim and oscillatory structural blade loads with accuracy comparable to that of existing free-wake models. However, they are unable to provide any information related to the wake structure, BVI locations, and noise. Finally, Van der Wall *et al* stated that, the frequency range within which finite-state inflow models are accurate for prediction of aeroelastic rotor blade loads, may reach up to 10P.

1.4 Real-time helicopter aeromechanics applications — Time-accurate aeroelasticity analysis

Real-time simulation requires that the unsteady behaviour of the aeroelastic rotor blades can be accurately predicted at a rate that is faster than that at which the dominant physical phenomena actually occur in nature. The dynamics of aeroelastic rotor blades have been routinely modeled in non-real-time comprehensive rotorcraft codes (UMARC, CAMRAD/JA, CAMRAD II, S4, RCAS, DYMORE, and HOST)[31,33] but have not been catered for so far in real-time aeromechanics applications. This is due to the significant computational overhead that is associated with high-fidelity modelling methods employed by comprehensive codes such as FEA, multi-body dynamics, and free-wake aerodynamics. This essentially prohibits the deployment of such methods in real-time aeromechanics applications which, among others, include; flight simulation, nonlinear control law design, and automatic flight control system development.

The advent of high-performance computing has constituted an enabling technology in terms of enhancing the design capabilities of comprehensive rotorcraft codes[34]. Recent advances in computing power along with the introduction of parallel processing, have inevitably resulted in a significant decrease in the computational overhead associated with comprehensive analysis methods[35]. Hu *et al*[36] investigated the potential to reduce the computational cost of comprehensive codes through the following two approaches; 1. implementation of numerically efficient algorithms utilising the fast multi-pole method for reducing software complexity, and 2. incorporation of parallel processing. Hu *et al* concluded that, an effective combination of these two methods may potentially result in nearly two orders of magnitude reduction in computational cost.

However, despite the aforementioned advances in computing technology, Ref. 31 demonstrated that modern state-of-the-art comprehensive rotorcraft codes are still considered to be very computationally intensive. This is despite the use of parallel processing and supercomputers in some cases. Due to this reason, comprehensive codes often include numerous simplifications to bring down the computational effort, predominantly related to the wake treatment. This inevitably has a substantial effect on the accuracy of the obtained results. It is therefore understood that, real-time simulation using comprehensive analysis on a typical personal computer without the employment of software parallelisation, is not yet feasible.

A significant difficulty that is encountered in the field of real-time and time-accurate aeroelasticity analysis, lies with regards to securing robustness and computational efficiency of the incorporated solution approach. The employed numerical algorithms have to be able to suppress potential instabilities caused by discretisation errors associated with the use of finite-differences. The traditional remedies for suppressing such instabilities in time-marching methods have been; (a) employment of very small time-steps, and (b) introduction of non-physical/artificial damping. However, in the context of real-time simulation, option (a) is not a viable solution due to the fact that computational time is inversely proportional to the employed time-step. This behaviour

https://doi.org/10.1017/S0001924000010496 Published online by Cambridge University Press

essentially prohibits applicability in real-time when using very small time-steps. Option (b) is not generally considered to be good practice either. This is because introducing non-physical damping may severely compromise the accuracy of the obtained solution, particularly considering cases where large values of damping are required for stable analysis.

It is therefore understood that, real-time aeroelasticity simulation essentially requires as an enabling technology the development and implementation of novel finite-difference schemes, suitable for the treatment of elastic blade motion in the time-domain. The employed differentiation algorithms need not only be second-order accurate in nature, but also inherently stable so as to suppress numerical instabilities without resorting to very small time-steps or artificial damping.

1.5 Scope of present work

In light of the aforementioned research in the existing literature, the general objective of this work is to develop a mathematical approach for the simulation of flexible rotor blade dynamics in real-time helicopter aeromechanics applications, with accuracy comparable to that of established non-real-time comprehensive analysis methods. As such, the proposed approach has to be applicable to the task of rotor design by providing reasonably accurate estimates of:

- Rotor blade resonant frequencies
- Aeroelastic rotor-aircraft trim performance
- Oscillatory structural blade loads
- Rotor induced vibration

The mathematical model proposed in this paper for the simulation of rotor blade aeroelasticity in real-time, is broadly arranged as follows; A Lagrangian method is initially deployed for the rapid estimation of natural vibration characteristics of rotor blades with nonuniform structural properties. Lagrange's equation of motion is applied to the kinematics of rotor blade flap/lag bending and torsion. Modal characteristics obtained from Bernoulli-Euler beam and classical torsional vibration theory, are utilised as assumed deformation functions. Closed form integral expressions are incorporated for each degree-of-freedom (DOF), describing the generalised centrifugal forces and moments acting on the blade in terms of normal coordinates.

A matrix/vector-based formulation is developed for the treatment of three-dimensional kinematics of elastic blades. The proposed approach retains all nonlinear inertial terms associated with large blade deflections and fuselage angular motions. In order to overcome the classical hurdles of time-accurate simulation and establish applicability in real-time, a novel second-order accurate finite-difference algorithm, originally developed for stable free-wake analysis[37], is employed for the numerical discretisation of elastic blade motion in the time-domain. Integral expressions are derived and provided, describing the time-dependent force and moment loads exerted by the main rotor on the aircraft fuselage. The developed rotor dynamics formulation is coupled with a finite-state induced flow model and an unsteady blade element aerodynamics model. The combined approach is implemented in a helicopter flight dynamics simulation code, thus devising an integrated simulation framework for real-time helicopter aeromechanics.

The aeroelastic behaviour of two full-scale helicopter rotors is investigated; the hingeless rotor of the MBB Bo105 and the articulated rotor of the Aerospatiale SA330. Analyses are performed in terms of rotor blade flap-lag-torsion natural frequencies, rotor trim control angles, oscillatory structural blade loads and vibratory flap bending moment at the rotor hub. Extensive comparisons are carried out with measurements conducted in wind tunnel and flight tests as well as with simulations

https://doi.org/10.1017/S0001924000010496 Published online by Cambridge University Press

performed with the non-real-time comprehensive code CAMRAD/JA[38,39]. The computational time requirements associated with the execution of the proposed model are thoroughly assessed.

2.0 THEORETICAL DEVELOPMENT

2.1 Natural vibration characteristics of helicopter rotor blades

A Lagrangian approach is formulated in order to obtain the natural vibration characteristics of helicopter rotor blades for flap-lag-torsion. The rotor blade is modelled as a continuous system of nonuniform radial distribution of mass $\rho A(r)$, polar moment of inertia $\rho I_p(r)$, flap/lag bending stiffness $EI^{flap/lag}(r)$, and torsional rigidity $GJ^{flap/lag}(r)$. The well-known disadvantages of previously established energy methods[40]are mitigated by employing modal characteristics obtained from classical theories as assumed deformation functions, instead of standard polynomial expressions. It is shown in Ref. 41 that, this approach leads to considerable savings in computational time since the calculated modal frequencies converge rapidly to definitive values using only a small number of assumed functions. This is due to them originating in classical theories which renders them excellent candidates for deployment in any method based on the principle of virtual work.

It is noted that, the DOFs corresponding to flap-lag-torsion are treated separately and thus neither inertial nor aeroelastic coupling is taken into account in the formulation of the Lagrangian eigenproblem. This is due to the fact that, the proposed approach is predominantly designated for dynamic response analysis in the time-domain. Thus, any aerodynamic or nonlinear inertial loads may be treated as a time-history of external forcing using Duhamel's integral to obtain the time-accurate dynamic response of the rotor blades.

2.1.1 Derivation of assumed deformation functions

A finite series of assumed deformation functions is required for each DOF in order to utilise the theory of Lagrangian kinematics[40]. These are obtained through application of classical Bernoulli-Euler beam and torsional vibration theory. In order to maintain generality in the proposed approach, an effective modal co-ordinate x is defined as the spatial independent variable based on the local blade radius $r \in (eR, R)$, where e is the hinge/root offset as a fraction of rotor blade radius R. The effective modal co-ordinate is defined as $x = r - eR, x \in (0,l)$ where $l = R(1 - e)$. This transformation is carried out due to a potential existence of an actual hinge/root blade offset from the centre of the rotor hub and is required in order to ensure proper application of boundary conditions.

The governing equation for the transverse displacement $w(x,t)$ of a non-rotating beam with variable bending stiffness $EI(x)$ and mass per unit length $\rho A(x)$, subjected to a vertical time varying distributed load per unit length $P(x,t)$, is a fourth order partial differential equation (PDE):

$$\frac{\partial^2}{\partial x^2}(EI(x)\frac{\partial^2 w(x,t)}{\partial x^2}) + \rho A(x)\frac{\partial^2 w(x,t)}{\partial t^2} = P(x,t) \qquad \ldots (1)$$

where t is time in seconds. The governing equation for the torsional deformation angle $\theta(x,t)$ of a non-rotating body with variable torsional rigidity $GJ(x)$ and polar moment of inertia per unit length $\rho I_p(x)$, subjected to torsional moment loads per unit length $M(x,t)$, is a second order PDE:

$$\frac{\partial}{\partial x}(GJ(x)\frac{\partial \theta(x,t)}{\partial x}) + M(x,t) = \rho I_p(x)\frac{\partial^2 \theta(x,t)}{\partial t^2} \qquad \ldots (2)$$

https://doi.org/10.1017/S0001924000010496 Published online by Cambridge University Press

At this point, uniform structural properties are assumed along with zero external forcing. Applying separation of variables in Equations (1) and (2) leads to the following solutions for the spatial parts $\Phi(x)$, $\Theta(x)$ of Equations (1), (2) respectively:

$$\Phi(x) = A\mathrm{Sin}\beta x + B\mathrm{Cos}\beta x + C\mathrm{Sin}\beta x + D\mathrm{Cos}\beta x \quad \ldots (3)$$

$$\Theta(x) = A\mathrm{Cos}\gamma x + B\mathrm{Sin}\gamma x \quad \ldots (4)$$

where β and γ are the natural frequency parameters corresponding to cases of transverse displacement and torsional deformation respectively[41]. Equations (3), (4) express the transverse displacement and torsional mode shapes with respect to an idealised structure. The parameters A, B, C and D are constants of integration that are determined through application of boundary conditions. The solution of Equations (3) and (4) was given in Ref. 41 for specific sets of boundary conditions corresponding to hingeless, freely-hinged and spring-hinged articulated rotor blades.

The aforementioned process provides the first N vibration mode shapes for the DOF's corresponding to flap/lag bending and torsion of a non-rotating structure with radially uniform structural properties. Translating the acquired mode shapes from the effective modal co-ordinate domain x to the local blade element radius domain r, essentially gives $\phi_i^{flap}(r)$, $\phi_i^{lag}(r)$, $\phi_i^{torsion}(r)$, $i = 1 \ldots N$. The acquired functions are orthogonal with one another, they satisfy the structure's boundary conditions, they approximate the actual mode shapes of the non uniform-rotating structure reasonably well[42] and their derivatives with respect to r are readily available analytically. Thus, they are excellent candidates for deployment as assumed deformation functions in Lagrangian kinematics.

2.1.2 Lagrangian formulation for nonuniform rotor blades

After a series of well-conditioned assumed deformation functions has been extracted from classical methods, Lagrangian kinematics can be utilised and the analysis can be extrapolated to the nonuniform rotating case. Lagrange's equation of motion for a system whose space configuration is governed by a finite series of time-dependent generalised co-ordinates $q_i(t)$, $i = 1 \ldots N$ is given by:

$$\frac{\mathrm{d}}{\mathrm{d}t}\left(\frac{\partial T}{\partial \dot{q}_i}\right) - \frac{\partial T}{\partial q_i} + \frac{\partial U}{\partial q_i} = Q_i, \quad i = 1,\ldots N \quad \ldots (5)$$

where T and U are the kinetic and strain energy of the system, while Q_i signifies the generalised external force corresponding to the ith co-ordinate. Expressing the time-dependent transverse displacement for flap-lag bending motion $w^{flap/lag}(r,t)$ along with the torsional deformation angle $\theta(r,t)$, in terms of the finite series of assumed modal functions obtained from classical methods, gives:

$$w^{flap}(r,t) = \sum_{i=1}^{N} \phi_i^{flap}(r) q_i^{flap}(t) \quad \ldots (6)$$

$$w^{lag}(r,t) = \sum_{i=1}^{N} \phi_i^{lag}(r) q_i^{lag}(t) \quad \ldots (7)$$

$$\theta(r,t) = \sum_{i=1}^{N} \phi_i^{torsion}(r) q_i^{torsion}(t) \quad \ldots (8)$$

https://doi.org/10.1017/S0001924000010496 Published online by Cambridge University Press

where $q_i^{flap}(t)$, $q_i^{lag}(t)$, and $q_i^{orsion}(t)$ are generalised co-ordinates expressing the contribution of the assumed modal functions on the blade's flap/lag transverse displacement and torsional deformation respectively. Assumption of small deformations allows for the linearisation of Lagrange's equation by effectively setting $\frac{\partial T}{\partial q_i} \approx 0$ in Equation (5)[40].

The system's strain and kinetic energy can be expressed in terms of generalised co-ordinates for the flap-lag-torsion DOFs as follows:

$$U^{flap/lag/torsion} = \frac{1}{2}\sum_{i=1}^{N}\sum_{j=1}^{N} k_{i,j}^{flap/lag/torsion} q_i^{flap/lag/torsion}(t) q_j^{flap/lag/torsion}(t) + \frac{1}{2}\sum_{i=1}^{N}\sum_{j=1}^{N} f_{i,j}^{flap/lag/torsion} q_i^{flap/lag/torsion}(t) q_j^{flap/lag/torsion}(t) \quad \ldots (9)$$

$$T^{flap/lag/torsion} = \frac{1}{2}\sum_{i=1}^{N}\sum_{j=1}^{N} m_{i,j}^{flap/lag/torsion} \dot{q}_i^{flap/lag/torsion}(t) \dot{q}_j^{flap/lag/torsion}(t) \quad \ldots (10)$$

The inter-modal coupling coefficients within Equations (9) and (10) are defined as:

$$m_{i,j}^{flap/lag} = \int_{eR}^{R} \rho A(r) \phi_i^{flap/lag}(r) \phi_j^{flap/lag}(r) \mathrm{d}r \quad \ldots (11)$$

$$k_{i,j}^{flap/lag} = \int_{eR}^{R} EI^{flap/lag}(r) \phi_{iq}^{''flap/lag}(r) \phi_j^{''flap/lag}(r) \mathrm{d}r \quad \ldots (12)$$

$$f_{i,j}^{flap/lag} = K^{flap/lag} \phi_i^{'flap/lag}(eR) \phi_j^{'flap/lag}(eR) \quad \ldots (13)$$

$$m_{i,j}^{torsion} = \int_{eR}^{R} \rho I_p(r) \phi_i^{torsion}(r) \phi_j^{torsion}(r) \mathrm{d}r \quad \ldots (14)$$

$$k_{i,j}^{torsion} = \int_{eR}^{R} GJ(r) \phi_i^{'torsion}(r) \phi_j^{'torsion}(r) \mathrm{d}r \quad \ldots (15)$$

$$f_{i,j}^{torsion} = K^{torsion} \phi_i^{torsion}(eR) \phi_j^{torsion}(eR) \quad \ldots (16)$$

where the superscripts $(\,)'$ and $(\dot{\,})$ signify differentiation with respect to r and t respectively. It is noted that the symbols; $m_{i,j}^{flap/lag}$, $k_{i,j}^{flap/lag}$ and $f_{i,j}^{flap/lag}$ essentially denote the inertial, elastic, and hub-spring inter-modal coupling coefficients respectively between the ith and jth assumed modes of motion for flap and lag transverse displacement. The inter-modal coupling coefficient $f_{i,j}^{flap/lag}$ is non-zero only with regards to the case of an articulated rotor with a specifically defined hub spring with stiffness $K^{flap/lag}$. The symbols $m_{i,j}^{torsion}$, $k_{i,j}^{torsion}$ and $f_{i,j}^{torsion}$ signify the corresponding inter-modal coupling coefficients for the case of torsional deformation. The term $f_{i,j}^{torsion}$ is non-zero only for the case of finite pitch control system torsional stiffness $K^{torsion}$.

A thorough kinematic analysis was carried out in Ref. 41 where closed form expressions were derived for the generalised centrifugal external force and moment loads as functions of generalised coordinates for each DOF. The derived expressions give:

https://doi.org/10.1017/S0001924000010496 Published online by Cambridge University Press

$$Q_i^{flap/lag/torsion} = -\sum_{j=1}^{N} I_{i,j}^{flap/lag/torsion} q_j^{flap/lag/torsion}(t), \quad i = 1,...N \qquad \ldots (17)$$

where the symbols $I_{i,j}^{flap}$, $I_{i,j}^{lag}$ and $I_{i,j}^{torsion}$ denote the centrifugal stiffening inter-modal coupling coefficients for flap-lag-torsion respectively. These were derived in closed form in Ref. 41 and are defined as follows:

$$I_{i,j}^{flap} = \int_{eR}^{R} \rho A(r) \Omega^2 r \int_{eR}^{r} \phi_i^{'flap}(\xi) \phi_j^{'flap}(\xi) \mathrm{d}\xi \mathrm{d}r \qquad \ldots (18)$$

$$I_{i,j}^{lag} = \int_{eR}^{R} \rho A(r) \Omega^2 r \int_{eR}^{r} \phi_i^{'lag}(\xi) \phi_j^{'lag}(\xi) \mathrm{d}\xi \mathrm{d}r - \int_{eR}^{R} \rho A(r) \Omega^2 \phi_i^{lag}(r) \phi_j^{lag}(r) \mathrm{d}r \qquad \ldots (19)$$

$$I_{i,j}^{torsion} = \int_{eR}^{R} \rho A(r) \Omega^2 Y_{offset}^2(r) \phi_i^{torsion}(r) \phi_j^{torsion}(r) \mathrm{d}r \qquad \ldots (20)$$

where Ω is the nominal shaft rotorspeed and $Y_{offset}(r)$ is the aerofoil's chordwise centre of mass offset from the blade elastic axis.

Substituting Equations (9) and (10) along with Equation (17) into the linearised version of Equation (5), and subsequently a assuming periodic solution of the form $q_i = \bar{q}_i \mathrm{Sin}(\omega_i t + \psi_i)$ for the generalised co-ordinates, leads to the formulation of the following linear system of equations:

$$\sum_{j=1}^{N} (G_{i,j}^{flap/lag/torsion} - (\omega_i^{flap/lag/torsion})^2 m_{i,j}^{flap/lag/torsion}) \bar{q}_j^{flap/lag/torsion} = 0, \quad i = 1,...N \qquad \ldots (21)$$

where $\omega_i^{flap/lag/torsion}$ is the natural frequency of the ith mode for flap, lag, and torsional vibration in that order. The parameter $\mathbf{GI}_{ij}^{flap/lag/torsion} = \mathbf{k}_{ij}^{flap/lag/torsion} + \mathbf{f}_{ij}^{flap/lag/torsion} + \mathbf{I}_{ij}^{flap/lag/torsion}$ may be viewed as the overall effective stiffness coupling coefficient between the ith and jth assumed modes of flap-lag-torsion including elastic $k_{i,j}$, hub-spring $f_{i,j}$ and centrifugal stiffening effects $I_{i,j}$.

Rearranging Equation (21) in matrix notation leads to the following expression:

$$\mathbf{A}_{Lagrange}^{flap/lag/torsion} \bar{\mathbf{q}}^{flap/lag/torsion} = 0 \qquad \ldots (22)$$

where $\bar{\mathbf{q}} = [\bar{q}_1, \bar{q}_2, \ldots \bar{q}_N]^T$ considering the cases of flap, lag, and torsional vibration respectively. $\mathbf{A}_{Lagrange}^{flap/lag/torsion}$ are square symmetric matrices of size N. The necessary condition for Equation (22) to have non-trivial solutions requires that $\det \mathbf{A}_{Lagrange}^{flap/lag/torsion} = 0$. This leads to a transcendental equation that can be evaluated numerically through marching within the corresponding flap-lag-torsion frequency domains until the first N values of $\omega_i^{flap/lag/torsion}$, $i = 1, \ldots N$ that provide non-trivial solutions for Equation (22) are obtained. The vectors $\bar{\mathbf{q}}_i^{flap}$, $\bar{\mathbf{q}}_i^{lag}$ and $\bar{\mathbf{q}}_i^{torsion}$ are eigenvectors of matrices $\mathbf{A}_{Lagrange}^{flap}$, $\mathbf{A}_{Lagrange}^{lag}$, and $\mathbf{A}_{Lagrange}^{torsion}$ and are associated with $\omega_i^{flap/lag/torsion}$, $i = 1, \ldots N$ respectively. It is noted that since $\mathbf{A}_{Lagrange}^{flap}$, $\mathbf{A}_{Lagrange}^{lag}$, and $\mathbf{A}_{Lagrange}^{torsion}$ are square symmetric matrices, their eigenvectors $\bar{\mathbf{q}}^{flap/lag/torsion}$ are orthogonal with one another when using the inertial inter-modal coupling coefficients $m_{i,j}^{flap/lag/torsion}$ for weighting.

The final N first mode shapes of the non-uniform rotating blade can be obtained from the dot products of the assumed mode shape vectors (that were obtained from classical methods) and the eigenvectors of $\mathbf{A}_{Lagrange}^{flap}$, $\mathbf{A}_{Lagrange}^{lag}$, and $\mathbf{A}_{Lagrange}^{torsion}$ respectively. This procedure is expressed as:

$$X_i^{flap/lag/torsion}(r) = \Phi^{flap/lag/torsion}(r) \cdot \bar{\mathbf{q}}_i^{flap/lag/torsion}, \quad i = 1,...N \qquad \ldots (23)$$

https://doi.org/10.1017/S0001924000010496 Published online by Cambridge University Press

where $\mathbf{\Phi(r)} = [\phi_j(r), j = 1, \ldots N]^T$ are the assumed mode shape vectors for flap-lag-torsion respectively. It was shown in Ref. 41 that the orthogonality between the acquired eigenvectors of matrices $\mathbf{A}^{flap}_{Lagrange}$, $\mathbf{A}^{lag}_{Lagrange}$, and $\mathbf{A}^{torsion}_{Lagrange}$ due to their symmetric nature, also leads to the orthogonality of the acquired mode shapes given by Equation (23).

2.2 Aeroelastic response of helicopter rotor blades

The modal content acquired in the previous section is now utilised in order to obtain the dynamic response of the flexible rotor blades to any time-history of external forcing. The three-dimensional kinematics of elastic blades are treated in detail and nonlinear acceleration terms associated with large deflections and rotor hub motions are rigorously retained. A novel, second-order accurate, backward-difference approximation scheme, originally developed for time-accurate free-wake analysis[37], is utilised for the finite-difference treatment of elastic blade motion in the time-domain. Implementation of the particular algorithms, not only results in increased simulation stability, but also in significant reduction of computational time which is a prerequisite for real-time simulation.

The end-product of the analysis is a set of integral equations describing the time-dependent forces and moments exerted by the elastic rotor blades on the aircraft fuselage, expressed in the hub-wind axes reference frame[3]. The generality and rigorousness of the proposed approach ensures compatibility with any quasi-steady or unsteady rotor wake inflow and blade element aerodynamics theory. The proposed mathematical model is provided in a highly-compact form that can be implemented in existing flight mechanics codes without any change in the offered expressions.

2.2.1 Treatment of three-dimensional kinematics of elastic blades

Capturing the nature of the aeroelastic response of the main rotor requires that the unsteady aerodynamic and inertial loads exerted on the blades are accurately modelled. A helicopter may encounter a wide variety of flight conditions which, among others, include; pitching, rolling, climbing, and turning. The inertial velocity and acceleration terms associated with the helicopter motion as well as the dynamic deformation of the elastic blades, need to be accounted for. Thus, an effective treatment of the rotor blade's nonlinear, three-dimensional kinematics is required.

Figure 1 presents the reference systems used in this paper for the description of three-dimensional kinematics of elastic blades. Each beam element $p(r,t)$ of radius r and differential mass $dm = \rho A(r)\, dr$, is placed on the blade's mean elastic axis as shown in Fig. 1(a). The centre of mass of $p(r,t)$ is set to be chord-wisely offset from the blade's elastic axis by an amount equal to $Y_{offset}(r)$. A global non-rotating reference frame O is defined, whose Z axis is aligned with the main rotor shaft. The origin of the O frame is located at the centre of the main rotor hub. The O frame's unit vectors $\mathbf{e}_x$, $\mathbf{e}_y$ and $\mathbf{e}_z$ are defined as shown in Fig. 1(a). The mathematical transformation between the unit vectors of the global O system and the hub-wind axes reference frame, is straightforward and was given in Ref. 41. The translational/angular velocity and acceleration components on the O reference frame axes due to the motion of the helicopter, are shown in Fig. 1(a) and are classified in vector notation as follows:

$$\mathbf{u}_o = [u_o \quad v_o \quad w_o]^T \qquad \ldots (24)$$

$$\dot{\mathbf{u}}_o = [\dot{u}_o \quad \dot{v}_o \quad \dot{w}_o]^T \qquad \ldots (25)$$

$$\boldsymbol{\omega}_o = [p_o \quad q_o \quad r_o]^T \qquad \ldots (26)$$

$$\dot{\boldsymbol{\omega}}_o = [\dot{p}_o \quad \dot{q}_o \quad \dot{r}_o]^T \qquad \ldots (27)$$

https://doi.org/10.1017/S0001924000010496 Published online by Cambridge University Press

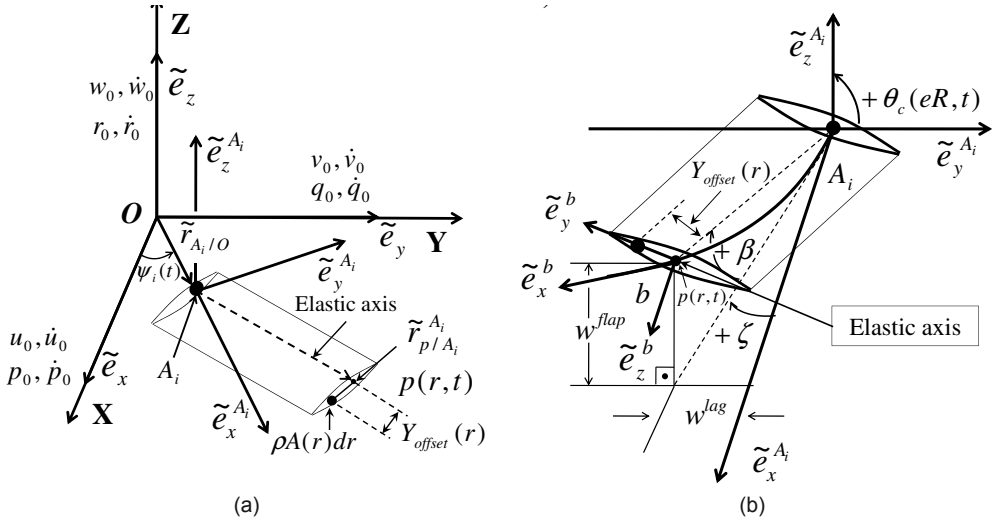


Figure 1. Reference systems used for the description of elastic blade kinematics: (a) Global non-rotating reference system *O*, (b) Rotating and blade element reference frames (A_i and *b* respectively).

A rotating reference system is defined for each of the N_b rotor blades as shown in Fig. 1(a). Each rotating frame A_i, $i = 1, \ldots N_b$ is aligned with the time-dependent root/hinge position of the corresponding blade. The origin of A_i is located at the *i*th blade root/hinge whose position vector is expressed in the non-rotating reference frame *O* as:

$$\mathbf{r}_{A_i/O} = \begin{Bmatrix} eR\mathrm{Cos}\psi_i(t) \\ eR\mathrm{Sin}\psi_i(t) \\ 0 \end{Bmatrix} \quad \ldots (28)$$

where $\psi_i(t)$ is the azimuth angle of the *i*th blade at time *t*. For a rotor employing predefined pre-cone, pre-sweep, and collective pitch angles, a transformation matrix A_i can be defined as:

$$\mathbf{A_i} = \mathbf{\Theta_0 B_{pre} Z_{pre} \Psi_i} \quad \ldots (29)$$

Matrix multiplication of A_i with any vector expressed in the global system *O*, will essentially produce the respective expression of the same vector in the rotating system A_i. The individual transformation matrices $\mathbf{\Theta}_0$, $\mathbf{B}_{pre}$, $\mathbf{Z}_{pre}$ and $\mathbf{\Psi}_i$ describe the rotations about the corresponding angles and have been provided in Ref. 41. It can be observed that only collective pitch $\mathbf{\Theta}_0$ has been applied during the process of aligning A_i with the blade root/hinge positioning. The effects of cyclic pitch, blade twist, and torsion will be accounted for within the rotating system A_i.

Expressing the absolute angular velocity and acceleration vectors of the origin of A_i in the non-rotating global system *O* yields:

$$\boldsymbol{\omega}_{A_i} = [p_o \quad q_o \quad (r_o + \Omega)]^T \quad \ldots (30)$$

$$\dot{\boldsymbol{\omega}}_{A_i} = [\dot{p}_o \quad \dot{r}_o \quad (\dot{q}_o + \dot{\Omega})]^T \quad \ldots (31)$$

https://doi.org/10.1017/S0001924000010496 Published online by Cambridge University Press

Thus, the absolute linear velocity and acceleration vectors of the origin of can be expressed in the non-rotating system *O* as follows:

$$\mathbf{u}_{A_i} = \mathbf{u}_o + \boldsymbol{\omega}_{A_i} \times \mathbf{r}_{A_i/O} \quad \ldots (32)$$

$$\mathbf{a}_{A_i} = \dot{\mathbf{u}}_o + \boldsymbol{\omega}_{A_i} \times (\boldsymbol{\omega}_{A_i} \times \mathbf{r}_{A_i/O}) + \dot{\boldsymbol{\omega}}_{A_i} \times \mathbf{r}_{A_i/O} \quad \ldots (33)$$

The position vector of each beam element $p(r,t)$ relative to the origin of A_i is illustrated in Fig. 1(b). It can be mathematically expressed in the rotating A_i reference system as:

$$\mathbf{r}_{p/A_i}^{A_i} = \begin{Bmatrix} (r-eR)\mathrm{Cos}\,\beta(r,t)\mathrm{Cos}\,\zeta(r,t) \\ -(r-eR)\mathrm{Sin}\,\zeta(r,t) \\ (r-eR)\mathrm{Sin}\,\beta(r,t) \end{Bmatrix} \quad \ldots (34)$$

It is noted that, $\beta(r,t)$ and $\zeta(r,t)$ are the time-dependent element equivalent flap and lag angles respectively. They are essentially defined in A_i as shown in Fig. 1(b) and can be expressed mathematically as:

$$\beta(r,t) = \mathrm{Arcsin}\frac{w^{flap}(r,t)}{r-eR} \quad \ldots (35)$$

$$\zeta(r,t) = \mathrm{Arcsin}\frac{w^{lag}(r,t)}{r-eR} \quad \ldots (36)$$

where $w^{flap/lag}(r,t)$ is the time-dependent blade transverse displacement as regards flap and lag motion respectively. The negative sign in front of the second element of $\mathbf{r}_{p/A_i}^{A_i}$ signifies the convention dictating positive $\zeta(r,t)$ for backwards blade transverse displacement (Fig. 1(b). The first and second temporal derivatives of Equations (35) and (36), lead to the respective angular velocity and acceleration components of beam element $p(r,t)$ expressed in A_i. The corresponding expressions for $\dot{\beta}(r,t)$ and $\ddot{\beta}(r,t)$ are given by:

$$\dot{\beta}(r,t) = \frac{\dot{w}^{flap}(r,t)}{\sqrt{(r-eR)^2 - w^{flap}(r,t)^2}} \quad \ldots (37)$$

$$\ddot{\beta}(r,t) = \frac{\ddot{w}^{flap}(r,t)}{\sqrt{(r-eR)^2 - w^{flap}(r,t)^2}} + \frac{w^{flap}(r,t)\cdot \dot{w}^{flap}(r,t)^2}{((r-eR)^2 - w^{flap}(r,t)^2)^{3/2}} \quad \ldots (38)$$

The determination of $\dot{\zeta}(r,t)$ and $\ddot{\zeta}(r,t)$ can be carried out using similar expressions.

Two specific cases are distinguished with respect to formulating the total angular velocity and acceleration vectors of beam element $p(r,t)$ in the rotating A_i reference frame. The distinction lies with regards to the radial position at which cyclic pitch is applied. For the case that cyclic pitch is applied inboard of the blade root/hinge location, the corresponding vectors are given by:

$$\boldsymbol{\omega}_{p/A_i}^{A_i} = \begin{Bmatrix} \dot{\theta}_c(eR,t) \\ -\dot{\beta}(r,t) \\ -\dot{\zeta}(r,t) \end{Bmatrix} \quad \ldots (39)$$

https://doi.org/10.1017/S0001924000010496 Published online by Cambridge University Press

$$\dot{\boldsymbol{\omega}}_{p/A_i}^{A_i} = \begin{Bmatrix} \ddot{\theta}_c(eR,t) \\ -\ddot{\beta}(r,t) \\ -\ddot{\zeta}(r,t) \end{Bmatrix} \quad \ldots (40)$$

As regards the case that cyclic pitch is applied outboard of the radial flap/lag blade hinge location, the corresponding expressions are re-written as:

$$\boldsymbol{\omega}_{p/A_i}^{A_i} = \begin{bmatrix} \mathrm{Cos}\hat{\beta}\,\mathrm{Cos}\hat{\zeta} & -\mathrm{Cos}\hat{\beta}\,\mathrm{Sin}\hat{\zeta} & \mathrm{Sin}\hat{\beta} \\ \mathrm{Sin}\hat{\zeta} & \mathrm{Cos}\hat{\zeta} & 0 \\ -\mathrm{Sin}\hat{\beta}\,\mathrm{Cos}\hat{\zeta} & \mathrm{Sin}\hat{\beta}\,\mathrm{Sin}\hat{\zeta} & \mathrm{Cos}\hat{\beta} \end{bmatrix}^{-1} \begin{Bmatrix} \dot{\theta}_c(eR,t) \\ 0 \\ 0 \end{Bmatrix} + \begin{Bmatrix} 0 \\ -\dot{\beta}(r,t) \\ -\dot{\zeta}(r,t) \end{Bmatrix} \quad \ldots (41)$$

$$\dot{\boldsymbol{\omega}}_{p/A_i}^{A_i} = \begin{bmatrix} \mathrm{Cos}\hat{\beta}\,\mathrm{Cos}\hat{\zeta} & -\mathrm{Cos}\hat{\beta}\,\mathrm{Sin}\hat{\zeta} & \mathrm{Sin}\hat{\beta} \\ \mathrm{Sin}\,\hat{\zeta} & \mathrm{Cos}\hat{\zeta} & 0 \\ -\mathrm{Sin}\hat{\beta}\,\mathrm{Cos}\hat{\zeta} & \mathrm{Sin}\hat{\beta}\,\mathrm{Sin}\hat{\zeta} & \mathrm{Cos}\hat{\beta} \end{bmatrix}^{-1} \begin{Bmatrix} \ddot{\theta}_c(eR,t) \\ 0 \\ 0 \end{Bmatrix} + \begin{Bmatrix} 0 \\ -\ddot{\beta}(r,t) \\ -\ddot{\zeta}(r,t) \end{Bmatrix} \quad \ldots (42)$$

where $\hat{\beta} = \beta(eR,t)$ and $\hat{\zeta} = \zeta(eR,t)$. It is noted that $\theta_c(eR,t)$ is the applied cyclic pitch angle at the blade root/hinge position eR at time t. Equations (39), (40) are suitable for the analysis of hingeless rotor blades with cantilever boundary conditions at the rotor hub. Equations (41), (42) are better-suited for articulated blades where cyclic pitch is applied outboard of the flap/lag hinge location. As such, they include the respective transformation of applied cyclic pitch about the local flap/lag angles ($\hat{\beta}$ / $\hat{\zeta}$) at the blade hub.

Equations (41) and (42) have been derived under the assumption of coincident flap and lag hinge locations. When considering different sequences of hinge arrangements, Equations (41) and (42) will have to be modified accordingly along with the employed assumed deformation functions in order to reflect the kinematics associated with the corresponding hinge sequence. It is also noted that, the cyclic pitch angle at the hub $\theta_c(eR,t)$ is usually expressed as a first harmonic periodic function of blade azimuth angle $\psi_i(t)$. Thus, its temporal derivatives can be easily evaluated in analytical closed form. Considering rotor configurations that incorporate higher harmonic control, the respective derivatives of $\theta_c(eR,t)$ can still be analytically evaluated in closed form and implemented in Equations (39) and (40) or Equations (41) and (42), depending on the boundary conditions at the rotor hub.

The relative linear velocity and acceleration vectors of element $p(r,t)$ relative to the origin of and expressed in the A_i rotating frame are given by:

$$\mathbf{u}_{p/A_i}^{A_i} = \boldsymbol{\omega}_{p/A_i}^{A_i} \times \mathbf{r}_{p/A_i}^{A_i} \quad \ldots (43)$$

$$\mathbf{a}_{p/A_i}^{A_i} = \boldsymbol{\omega}_{p/A_i}^{A_i} \times (\boldsymbol{\omega}_{p/A_i}^{A_i} \times \mathbf{r}_{p/A_i}^{A_i}) + \dot{\boldsymbol{\omega}}_{p/A_i}^{A_i} \times \mathbf{r}_{p/A_i}^{A_i} \quad \ldots (44)$$

which along with $\mathbf{r}_{p/A_i}^{A_i}$ they can be expressed in the global non-rotating O frame of reference using the following transformations:

$$\mathbf{r}_{p/A_i}^{O} = \mathbf{A}_i^{-1} \mathbf{r}_{p/A_i}^{A_i} \quad \ldots (45)$$

$$\mathbf{u}_{p/A_i}^{O} = \mathbf{A}_i^{-1} \mathbf{u}_{p/A_i}^{A_i} \quad \ldots (46)$$

https://doi.org/10.1017/S0001924000010496 Published online by Cambridge University Press

$$\mathbf{a}_{p/A_i}^{O} = \mathbf{A}_i^{-1}\mathbf{a}_{p/A_i}^{A_i} \quad \ldots (47)$$

The absolute velocity and acceleration vectors of element $p(r,t)$ are given in the global non-rotating reference frame O as follows:

$$\mathbf{u}_p^O = \mathbf{u}_{A_i} + \mathbf{u}_{p/A_i}^O + \boldsymbol{\omega}_{A_i} \times \mathbf{r}_{p/A_i}^O \quad \ldots (48)$$

$$\mathbf{a}_p^O = \mathbf{a}_{A_i} + \mathbf{a}_{p/A_i}^O + 2 \cdot \boldsymbol{\omega}_{A_i} \times \mathbf{u}_{p/A_i}^O + \dot{\boldsymbol{\omega}}_{A_i} \times \mathbf{r}_{p/A_i}^O + \boldsymbol{\omega}_{A_i} \times (\boldsymbol{\omega}_{A_i} \times \mathbf{r}_{p/A_i}^O) \quad \ldots (49)$$

The inertial velocity and acceleration components can now be expressed in a blade element fixed frame of reference. Figure 1(b) demonstrates the local blade element system that corresponds to element $p(r,t)$ of the ith blade. The orientation of the local system is specified by unit vectors $\mathbf{e}_x^b$, $\mathbf{e}_y^b$ and $\mathbf{e}_z^b$. The vector $\mathbf{e}_x^b$ is defined so that it is coincident with the elastic axis of the deformed blade, pointing radially outwards. The $\mathbf{e}_y^b$ vector points towards the element's trailing edge and $\mathbf{e}_z^b$ completes the orthonormal system. Vector translation to a locally fixed blade element frame of reference, not only provides the inertial local flow-field conditions which is necessary input for any aerodynamic theory, but it also enables for D'Alembert's principle of superposition to be employed with respect to the aerodynamic and inertial blade loads.

Conversion of the global velocity and acceleration vectors given by Equations (48) and (49) to the local blade element co-ordinate system, can be achieved through the following transformation:

$$\mathbf{u}_p^b = \mathbf{T}_i^b \mathbf{u}_p^O \quad \ldots (50)$$

$$\mathbf{a}_p^b = \mathbf{T}_i^b \mathbf{a}_p^O \quad \ldots (51)$$

The matrix $\mathbf{T}_i^b$ essentially represents a tensor operator that relates any vector expressed in the global non-rotating reference frame O, directly to the local blade element co-ordinate system b of point $p(r,t)$ located on the ith blade. It can be defined as the following sequence of rotations:

$$\mathbf{T}_i^b = \begin{bmatrix} 1 & 0 & 0 \\ 0 & -1 & 0 \\ 0 & 0 & -1 \end{bmatrix} \boldsymbol{\theta}_c \boldsymbol{\beta} \boldsymbol{\zeta} \boldsymbol{\theta}_{torsion} \boldsymbol{\theta}_{tw} \boldsymbol{\lambda} \mathbf{A}_i \quad \ldots (52)$$

where λ, θ_{tw}, $\theta_{torsion}$, ζ, β, and θ_c are rotation matrices corresponding to the blade element sweep, pre-twist, torsion, lag, flap, and cyclic pitch angle at the hub respectively. These matrices are provided in Ref. 41. It is noted that, the applied sequence of rotations described by Equation (52) is valid for cases that cyclic pitch is applied inboard of the flap/lag hinge location. It is therefore suitable for the analysis of hingeless rotors. As regards the case of articulated blades where cyclic pitch is applied outboard of the flap/lag hinge, the respective sequence of rotations is given by:

$$\mathbf{T}_i^b = \begin{bmatrix} 1 & 0 & 0 \\ 0 & -1 & 0 \\ 0 & 0 & -1 \end{bmatrix} \begin{bmatrix} \mathrm{Cos}\hat{\beta}\,\mathrm{Cos}\hat{\zeta} & -\mathrm{Cos}\hat{\beta}\,\mathrm{Sin}\hat{\zeta} & \mathrm{Sin}\hat{\beta} \\ \mathrm{Sin}\hat{\zeta} & \mathrm{Cos}\hat{\zeta} & 0 \\ -\mathrm{Sin}\hat{\beta}\,\mathrm{Cos}\hat{\zeta} & \mathrm{Sin}\hat{\beta}\,\mathrm{Sin}\hat{\zeta} & \mathrm{Cos}\hat{\beta} \end{bmatrix}^{-1} \boldsymbol{\theta}_c \boldsymbol{\beta} \boldsymbol{\zeta} \boldsymbol{\theta}_{torsion} \boldsymbol{\theta}_{tw} \boldsymbol{\lambda} \mathbf{A}_i \quad \ldots (53)$$

https://doi.org/10.1017/S0001924000010496 Published online by Cambridge University Press

2.2.2 Finite-difference approximation of elastic blade motion in the time-domain

Determination of the first and second temporal derivatives of $\beta(r,t)$ and $\zeta(r,t)$ requires differentiation of w^{flap} and w^{fag} with respect to time. Ensuring applicability of the proposed modelling approach in the time-domain dictates numerical discretisation of elastic blade motion. As elaborated in the Introduction section of this paper, real-time simulation requires as an enabling technology the development and implementation of novel finite-difference schemes. These algorithms need not only be second-order accurate in nature, but also inherently stable so as to suppress numerical instabilities without resorting to very small time-steps or non-physical damping.

Within this work, a novel, second-order accurate, backward difference approximation scheme with established success in the field of time-accurate free-wake analysis[37], is employed for the evaluation of the temporal derivatives of interest. The corresponding finite-difference algorithm can be written as:

$$\frac{\partial w^{flap/lag}(r,t+\Delta t/2)}{\partial t} \approx \frac{3w^{flap/lag}(r,t+\Delta t)-w^{flap/lag}(r,t)-3w^{flap/lag}(r,t-\Delta t)+w^{flap/lag}(r,t-2\Delta t)}{4\Delta t} \quad \ldots (54)$$

where Δt is the employed time-step during time-marching. A linearised stability analysis has been carried out by Bhagwat and Leishman[37] with regards to the properties of Equation (54), where it has been shown that it is stable with positive damping.

Equation (54) provides the first temporal derivatives of $w^{flap/lag}$ at the time instant corresponding to $t+\Delta t/2$. Application of Equation (54) on the first temporal derivatives of $w^{flap/lag}$ taken at $t+\Delta t/2$, $t-\Delta t/2$, $t-3\Delta t/2$, etc, essentially provides the second temporal derivative of displacement at time = t. However, the present numerical approach requires knowledge of both first and second temporal derivatives of blade displacement at the same time instant. In order to rectify this inconsistency between the first and second derivatives of interest, the finite-difference approximation expressed by Equation (54) is modified by assuming $w^{flap/lag}(r,t+\Delta t/2) \approx \frac{w^{flap/lag}(r,t)+w^{flap/lag}(r,t+\Delta t)}{2}$.

The modified algorithm essentially provides the first temporal derivative at time = t and can be expressed in closed form as follows:

$$\frac{\partial w^{flap/lag}(r,t)}{\partial t} \approx \frac{3w^{flap/lag}(r,t+\Delta t)+2w^{flap/lag}(r,t)}{8\Delta t} + \frac{-4w^{flap/lag}(r,t-\Delta t)-2w^{flap/lag}(r,t-2\Delta t)+w^{flap/lag}(r,t-3\Delta t)}{8\Delta t} \quad \ldots (55)$$

The nature of both modified and original numerical differentiation schemes is illustrated in Fig. 2. It can be shown that Equation (55) also exhibits second-order accuracy with respect to time. Considering the approximation of the second temporal derivatives of $w^{flap/lag}(r,t)$ at time t, the original scheme can be deployed. This process can be expressed as:

https://doi.org/10.1017/S0001924000010496 Published online by Cambridge University Press

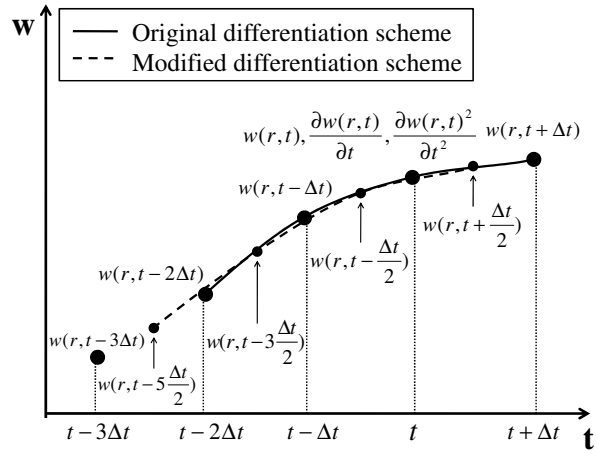


Figure 2. Graphical illustration of the employed numerical differentiation schemes.

$$\frac{\partial^2 w^{flap/lag}(r,t)}{\partial t^2} \approx \frac{3\dot{w}^{flap/lag}(r,t+\Delta t/2)-\dot{w}^{flap/lag}(r,t-\Delta t/2)-3\dot{w}^{flap/lag}(r,t-3\Delta t/2)+\dot{w}^{flap/lag}(r,t-5\Delta t/2)}{4\Delta t} \quad \ldots (56)$$

where the values of $\dot{w}^{flap/lag}$ in Equation (56) can be evaluated at their respective time instants using the original algorithm given by Equation (54). The aforementioned process is also applied for the approximation of the first and second temporal derivatives of $\theta(r,t)$ that are used later in this paper.

The superior stability of the employed finite-difference algorithms[37], essentially translates to the stability and robustness of the proposed mathematical approach. It is noted that, initial versions of the formulation that incorporated typical second-order central finite-differences, exhibited significant instabilities and thus required very small time-steps for stable simulation. This essentially prohibited applicability of the proposed approach in real-time. However, the employed schemes given by Equations (55) and (56) have essentially alleviated the aforementioned issues and stable simulations can be performed with time-steps leading to equivalent azimuth-steps of the order to 15º-20º. Thus, utilisation of the particular algorithms, not only results in increased simulation stability but also in significant reduction of computational time. This essentially constitutes an enabling technology for application of the developed aeroelastic rotor model in real-time.

2.2.3 Numerical integration of aeroelastic rotor blade loads

Considering the integration of aeroelastic blade loads, Equation (51) can be used for the evaluation of inertial acceleration terms directly in the local blade element frame of reference *b*. Using D'Alembert's principle of superposition for the inertial and aerodynamic loads, and subsequently converting them from the local element system *b* to the global non-rotating reference frame *O* gives:

$$d\mathbf{f}_p^O = [\mathbf{T}_i^b]^{-1}\{\mathbf{f}_{aero}^b - \rho A(r)\mathbf{a}_p^b\}dr \quad \ldots (57)$$

$$d\mathbf{m}_p^O = [\mathbf{T}_i^b]^{-1}\{\mathbf{m}_{aero}^b - \rho I_p(r)\ddot{\theta}_{torsion} - \rho A(r)\{\mathbf{r}_p^{b,offset}\times\mathbf{a}_p^b\}\}dr \quad \ldots (58)$$

https://doi.org/10.1017/S0001924000010496 Published online by Cambridge University Press

where $\ddot{\theta}_{\mathbf{torsion}} = [\ddot{\theta}(r,t)\ 0\ 0\ ]^T$ and $\mathbf{r}_p^{b,offset} = [0\ Y_{offset}(r)\ 0\ ]^T$. It is noted that $\mathbf{r}_p^{b,offset}$ essentially denotes the aerofoil centre of mass offset vector from the blade elastic axis expressed in the local element co-ordinate system. The vectors $\mathbf{f}_{aero}^b$ and $\mathbf{m}_{aero}^b$ describe the aerodynamic forces and moments per unit length respectively. These can be obtained using any blade element aerodynamic theory. The total forces and moments exerted by the main rotor hub on the aircraft fuselage can be expressed as the summation of contributions from the individual blades:

$$\mathbf{F}_{rotor}^O(t) = \sum_{i=1}^{N_b} \mathbf{F}_i^O(t) \qquad \ldots (59)$$

$$\mathbf{T}_{rotor}^O(t) = \sum_{i=1}^{N_b} \mathbf{T}_i^O(t) \qquad \ldots (60)$$

where:

$$\mathbf{F}_i^O(t) = \int_{eR}^{R} d\mathbf{f}_p^O, \quad i = 1,\ldots N_b \qquad \ldots (61)$$

The total moment that a rotor blade with a root connection (or hinge for a hinged blade) offset exercises about the origin of O can be expressed as:

$$\mathbf{T}_i^O(t) = \mathbf{T}_{i,offset}^O(t) + \mathbf{T}_{i,root}^O(t), \quad i = 1,\ldots N_b \qquad \ldots \qquad (62)$$

where $\mathbf{T}_{i,offset}^O(t)$ is the moment that the blade root/hinge applies about the origin O due to its force vector $\mathbf{F}_i^O(t)$ being offset from the centre of rotation by $\mathbf{r}_{A_i/O}$. It is given by:

$$\mathbf{T}_{i,offset}^O(t) = \mathbf{r}_{A_i/O} \times \mathbf{F}_i^O(t), \quad i = 1,\ldots N_b \qquad \ldots \qquad (63)$$

$\mathbf{T}_{i,root}^O(t)$ is the moment that the blade exerts directly on its root/hinge due to the root/hinge spring stiffness. For a hingeless rotor blade, the component $\mathbf{T}_{i,root}^O(t)$ is due to the effective stiffness of the elastometric elements at the blade root connection and can be expressed as:

$$\mathbf{T}_{i,root}^O(t) = \int_{eR}^{R} \mathbf{r}_{p/A_i}^O \times d\mathbf{f}_p^O + \int_{eR}^{R} d\mathbf{m}_p^O, \quad i = 1,\ldots N_b \qquad \ldots \qquad (64)$$

For spring-hinged articulated rotor blades, $\mathbf{T}_{i,root}^O(t)$ is essentially determined by the local flap/lag angles $\beta(eR,t)$, $\zeta(eR,t)$ and the corresponding spring stiffness constants $K^{flap/lag}$. For a freely-hinged articulated rotor, the blade cannot exert any moment at its hinge about the corresponding degree of freedom for which there is no spring or root stiffness involved.

The rotor force and moment vectors given by Equations (59) and (60) can be expressed in the hub-wind axes system using the transformations provided in Ref. 41. The final expressions can be used directly by any helicopter aeromechanics application for the calculation of the time-dependent three-dimensional rotor force and moment loads exerted on the aircraft.

2.3 Integrated aeroelastic rotor-airframe model

Figure 3 presents a block diagram that describes the modelling approach followed in this paper in order to formulate a complete aeroelastic rotor model for real-time simulation. The numerical methods described in the previous sections are combined to develop a complete structural formulation that covers the rotor dynamics aspect of the aeroelastic blade response problem. The combined approach is coupled with the Peters-He finite-state induced flow model[30,29] and the Leishman-Beddoes unsteady nonlinear blade element aerodynamics model[43]. Experimentally derived quasi-steady aerofoil data extracted from Ref. 44, have been used for the calibration of

https://doi.org/10.1017/S0001924000010496 Published online by Cambridge University Press

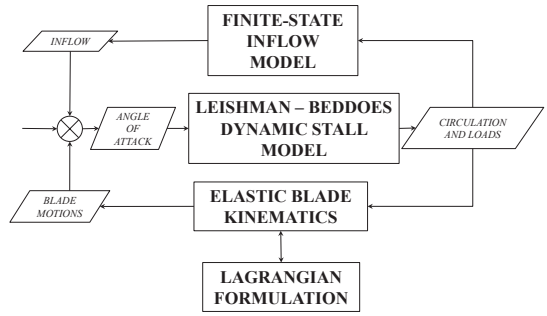


Figure 3. Aeroelastic rotor blade model block diagram.

the Leishman-Beddoes model. Careful treatment of induced flow terms arising from shed wake circulation has been carried out so that they are not duplicated by both induced flow and unsteady aerodynamics models.

The modal characteristics obtained from the Lagrangian approach are utilised. The dynamic response of the elastic blades is estimated using a fifth-order accurate numerical evaluation scheme of the convolution integral based on Simpson's rule. A complete aeroelastic rotor model is thus formulated. The linearised inertial terms accounted for in the derivation of natural vibration characteristics are excluded from the dynamic response analysis. This is done in order to avoid duplication of inertial loads in the forcing functions. However, these terms have to be accounted for when calculating the forces and moments exerted by the elastic blades on the rotor hub Equations (57) and (58).

The aircraft fuselage is treated dynamically as a rigid body with six degrees of freedom (three translations and three rotations) using the inertial tensors and mass value provided in Ref. 3. Experimentally derived look-up tables, also extracted from Ref. 3, are employed for the estimation of fuselage force and moment coefficients as functions of incidence and sideslip angles. Look-up tables are utilised for the prediction of the aerodynamic behaviour of the horizontal and vertical stabilisers. Steady-state aerofoil characteristics along with first-order dynamic inflow[10,11], are used for the prediction of tail-rotor performance. Rotor-fuselage aerodynamic interaction is accounted for by applying an incompressible potential flow/panel method on the three-dimensional geometry of the helicopter fuselage. The steady-state induced velocity perturbations arising from the presence of the fuselage are superimposed upon the main rotor inflow. This methodology has been extensively described in Ref. 41.

A globally convergent Newton-Raphson method is incorporated in order to obtain rotor trim, for either wind tunnel simulation with prescribed hub moments, or for designated sets of flight conditions. The numerical scheme is applied for the solution of Euler's nonlinear equations of motion for rigid body kinematics applied to the aircraft fuselage. The corresponding objective function for trim dictates minimisation of residual forces and moments about the fuselage centre of mass[3]. The main and tail rotors are marched simultaneously in time using the initial condition of nonexistent circulatory wake. The time-marching process continues until once-per-rev (1P) periodicity is achieved with respect to the main rotor flap/lag mean and first harmonic multi-blade co-ordinates; β_o, β_{1c}, β_{1s}, ζ_o, ζ_{1c} and ζ_{1s}. Having achieved quasi-steady periodic conditions in the aeroelastic rotor response, a finite series of rotations is carried out where the main rotor forces and moments are averaged in time in order to obtain mean values to be used for the nonlinear trim procedure.

https://doi.org/10.1017/S0001924000010496 Published online by Cambridge University Press

Table 1
Basic design parameters for the hingeless rotor of the MBB Bo105 helicopter

Design parameter	Value	Unit
Number of blades	4	—
Blade radius	4·91	m
Blade chord	0·27	m
Blade twist	8	degrees
Rotorspeed	44·4	rad/sec
Pre-cone	2·5	deg
Solidity	0·07	—
Aerofoil section	NACA 23012	—

Table 2
Basic design parameters for the articulated rotor of the Aerospatiale SA 330 helicopter

Design parameter	Value	Unit
Number of blades	4	—
Blade radius	7·54	m
Blade chord	0·54	m
Blade twist	8	degrees
Rotorspeed	27	rad/sec
Pre-cone	0	deg
Solidity	0·09	—
Aerofoil section	NACA 0012	—

3.0 RESULTS AND DISCUSSION

The integrated aeroelastic rotor-airframe model described in this paper was applied towards the investigation of the aeroelastic behaviour of two full-scale helicopter rotors; the hingeless rotor of the MBB Bo105 and the articulated rotor of the Aerospatiale SA330. Analyses were performed for rotor blade resonant frequencies, trim control angles, oscillatory structural blade loads, and vibratory flap bending moment at the rotor hub. The basic design parameters of the Bo105[45] and SA330[46] helicopter rotors are provided in Tables 1 and 2 respectively. Simulations were carried out for a wide range of advance ratios ($\mu = \frac{V}{\Omega R}$). A total number of eight inflow harmonics were deployed in an effort to capture the effect of higher harmonic loading on rotor inflow response. The radial inflow distribution polynomials used, reach up to the power of non-dimensional rotor radius. This inflow model configuration resulted in a finite-state model with 62 flow-states. A total of six flap-lag-torsion modes were employed in the respective rotor dynamics model.

Extensive comparisons were carried out with experimental data from wind tunnel and flight test measurements reported in Refs 46-48. With reference to the Bo105 rotor blade loads predictions, the main rotor was numerically trimmed to produce prescribed values of thrust and hub moments corresponding to a specific advance ratio μ and shaft angle α relative to the free-stream flow.

https://doi.org/10.1017/S0001924000010496 Published online by Cambridge University Press

Table 3
Summary of wind tunnel and flight test conditions for the Bo105 rotor (Figs 7-15)

Test type	μ	a	C_t/σ	C_l/σ	C_m/σ
Wind tunnel	0·197	−4·8°	0·071	–0·00053	0·00159
Wind tunnel	0·313	−9·6°	0·071	–0.00102	0·00074
Flight	0.197	−4·0°	0·071	–0·00039	0·00155
Flight	0·225	−4·8°	0·071	–0·00054	0·00154
Flight	0·306	−7·7°	0·071	–0·00089	0·00148

This was done in order for the simulated experiments to comply with the flight and wind tunnel testing procedures reported in Ref. 48. These are summarised in Table 3. Considering the SA330 rotor blade loads predictions, comparisons were only carried out with flight test data reported in Ref. 46. Predictions of oscillatory loads were therefore extracted from complete aeroelastic rotor-airframe trim calculations, instead of using designated values of thrust and hub moments.

Predictions of oscillatory blade loads made with the non-real-time comprehensive code CAMRAD/JA (Johnson Aeronautics)[38,39], are also compared with the real-time modelling approach of this paper. All CAMRAD/JA results were extracted from Refs 48 and 46 for the Bo105 and SA330 rotor respectively. It is noted that, the rotor dynamics formulation of CAMRAD/JA is based on engineering beam theory for rotating wings with large pitch and pre-twist angles. The rotor blade is modeled as a cantilever beam with a straight, undeformed elastic axis. Second-order lifting-line theory is deployed coupled with quasi-steady, two-dimensional aerofoil characteristics for the blade aerodynamic response. Corrections are applied for unsteady and three-dimensional flow effects[8]. A free-wake model is employed for the prediction of induced flow[27] which accounts for the wake's self-induced distortion using a discretised representation of the three-dimensional vortex wake. CAMRAD/JA is described extensively in Refs 38 and 39.

3.1 Modal analysis of rotor blades

Figure 4 presents the calculated resonance charts for the hingeless rotor of the Bo105 and the articulated rotor of the SA330 helicopter. Simulation results from Boeing-Vertol's computer code Y-71[45] for the Bo105 rotor blade with regards to flap/lag bending and torsional vibration natural frequencies at nominal rotorspeed, are also annotated in Fig. 4(a). Results from nonlinear analysis performed using CAMRAD [38] for the corresponding resonant frequencies of the SA330 rotor blade at nominal rotorspeed, are also included in Fig. 4(b). The frequency predictions made with Boeing-Vertol Y-71 and CAMRAD were extracted from Refs 45 and 46, respectively. The solid and broken lines correspond to predictions made with the Lagrangian formulation of this paper (Lagr.) while the markers denote either Y-71 or CAMRAD analysis, depending on figure.

Good agreement between Lagrangian predictions and Y-71 analysis can be observed in Fig. 4 (a) with respect to the blade's resonant frequencies at nominal rotorspeed ($\Omega = 44{\cdot}4$ rad/sec) for the hingeless rotor of the Bo105 helicopter. A small deviation is noted considering the natural frequency of the second torsion mode (2T). This is attributed to absence of elastic and inertial modal coupling in the Lagrangian eigenproblem. Good agreement between the Lagrangian approach and CAMRAD calculations can be noted in Fig. 4(b) with respect to flap (1F-3F), lag (1L-2L), and torsion (1T) resonant frequencies at nominal rotorspeed ($\Omega = 27$ rad/sec) for the articulated rotor blade of the SA330 helicopter.

https://doi.org/10.1017/S0001924000010496 Published online by Cambridge University Press

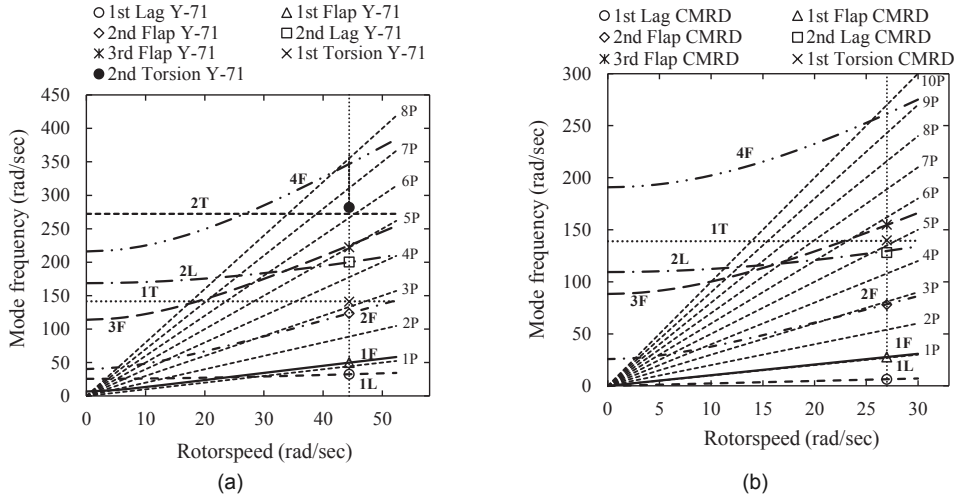


Figure 4. Calculated resonance charts – Lines denote Lagrangian predictions: (a) MBB Bo105 helicopter main rotor blade – Comparison with Boeing-Vertol Y-71 calculations from Ref. 45, (b) SA330 helicopter main rotor blade – Comparison with CAMRAD calculations from Ref. 46.

The relative difference in resonant frequencies between Lagrangian predictions and nonlinear analysis (Y-71 and CAMRAD) is consistently below 1%. However, the corresponding difference in the predicted frequency of the second torsion mode (2T) of the Bo105 rotor blade, reaches approximately 3% for the reasons elaborated above. The obtained natural frequencies along with the corresponding mode shapes (not shown in this paper for brevity) were utilised within this work for the estimation of the rotor blades' dynamic response to aerodynamic and nonlinear inertial external forcing. Finally it is emphasised that, the total computational time required for modal analysis using the proposed approach reaches roughly half a second on a typical personal computer.

3.2 Helicopter trim analysis

In this section, the model's ability to produce sound predictions of rotor trim control angles is examined. The underlying reason is that, good predictive ability in terms of trim controls essentially indicates the sound estimation of the aeroelastic rotor response to 1P harmonic excitation. The trim procedure was therefore initially validated with experimental data in terms of control angles for both helicopter models. It is noted that, the aerodynamic behaviour of the fuselage and the incorporated horizontal/vertical stabilisers, was estimated based on experimentally derived look-up tables extracted from Ref. 3. Thus, any modelling uncertainties introduced through the imposed values of hub moments required for trimmed flight, were relatively limited. This was essential for the sound comparison of in-flight oscillatory structural blade loads, since the 1P moment components at the rotor hub need to be accurately prescribed as elaborated in Ref. 48.

Figures 5 and 6 present main rotor trim controls and power requirement predictions obtained from simulations performed for the Bo105 and the SA330 helicopters respectively. Results are presented for straight and level flight. The numerical method discussed in Section 2.3 Integrated aeroelastic rotor-airframe model of this paper was utilised in order to acquire trim solutions based on the aeroelastic behaviour of both helicopter rotors. Results are presented as functions of advance ratio ($\mu = \frac{V}{\Omega R}$) from hover ($\mu = 0$) to high-speed flight ($\mu \approx 0{\cdot}4$). Flight test data extracted from Refs

https://doi.org/10.1017/S0001924000010496 Published online by Cambridge University Press

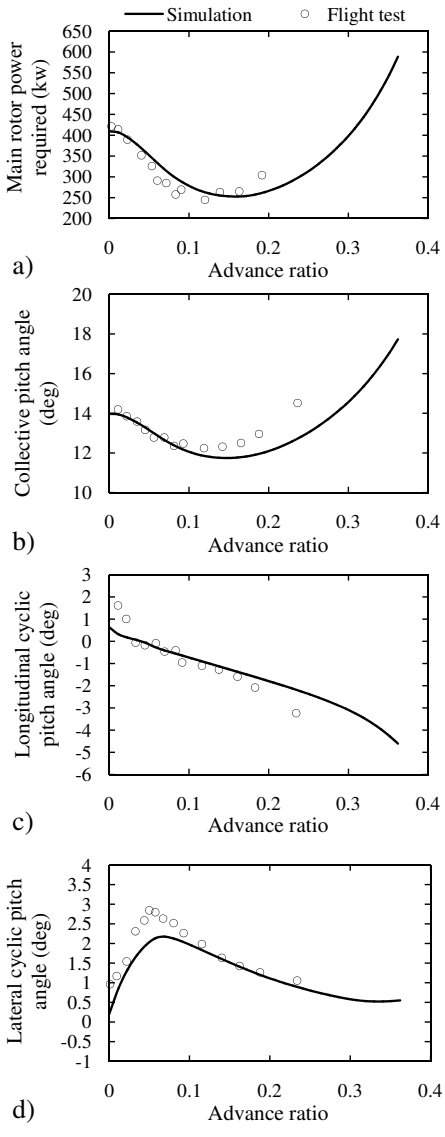


Figure 5. Main rotor trim parameters for the Bo105 helicopter – Comparison with flight test data from Ref. 47: (a) Power requirement P_{rotor}, (b) Collective pitch angle θ_0, c) Longitudinal cyclic pitch angle θ_{1s}, (d) Lateral cyclic pitch angle θ_{1c}.

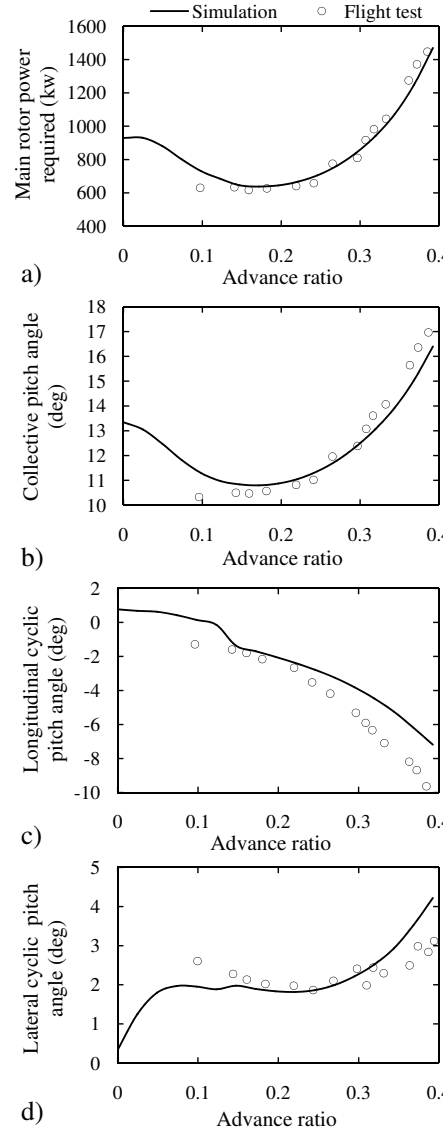


Figure 6. Main rotor trim parameters for the SA330 helicopter – Comparison with flight test data from Ref. 46: (a) Power requirement P_{rotor}, (b) Collective pitch angle θ_0, (c) Longitudinal cyclic pitch angle θ_{1s}, (d) Lateral cyclic pitch angle θ_{1c}.

46 and 47 for the Bo105 and the SA330 helicopter respectively, are also included for validation.

Good agreement between simulations and flight test data can be observed with respect to main rotor power requirement P_{rotor} and collective pitch angle θ_0, with regards to both investigated helicopter configurations. Considering the Bo105 model, agreement between predictions and measurements is best for $\mu \leq 0{\cdot}15$ (Figs 5 (a) and (b)). A relative deviation at higher values of μ is attributed to a potential overestimation of airframe drag. With respect to the SA330 model,

https://doi.org/10.1017/S0001924000010496 Published online by Cambridge University Press

better agreement is observed for $\mu \geq 0{\cdot}15$ (Figs 6(a) and (b). The deviation between predictions and measurements at low-speed flight is attributed to a potential overestimation of induced losses.

Good agreement can also be noticed between predictions and flight test data, considering both cyclic control inputs (θ_{1s} and θ_{1c}) within the range of μ for which results are presented. Considering the SA330 model, Figs 6(c) and (d) demonstrate that, according to simulation, rotor wake impingement on the horizontal stabiliser occurs for $\mu \geq 0{\cdot}15$ leading to large positive fuselage pitching moment. The control system thus compensates with a decrease in the longitudinal cyclic pitch control angle θ_{1s} as shown in Fig. 6(c). The flight test data suggests that, rotor wake impingement begins for lower advance ratios ($\mu \geq 0{\cdot}1$), since no required decrease is observed in θ_{1s} for $\mu \geq 0{\cdot}1$.

A noticeable deviation is observed between the predicted and measured lateral cyclic pitch angle θ_{1c} for $\mu \leq 0{\cdot}1$ considering both helicopter configurations. This essentially reveals the requirement for more sophisticated wake modelling regarding the transitional flight region ($0 \leq \mu \leq 0{\cdot}1$). The strong influence of the wake roll-up on the main rotor induced flow during transition from hover to forward flight, is not accounted for by the Peters-He inflow model which essentially models a skewed cylindrical wake. This deficiency leads to the underprediction of θ_{1c} at lower values of μ as shown in Figs 5(d) and 6(d).

The overall predictive qualities exhibited by the proposed aeroelastic rotor-airframe model in terms of rotor trim control angles, indicate its sound ability to estimate the quasi-steady rotor response to 1P harmonic excitation. The devised methodology may therefore be deployed for comparisons of oscillatory structural blade loads with measurements conducted in flight tests. This conclusion is valid for $\mu \geq 0{\cdot}1$ where the wake roll-up effect on induced flow is diminished and the Peters-He inflow model can be used with confidence for prediction of aeroelastic rotor loads.

3.3 Prediction of oscillatory structural blade loads

3.3.1 Comparison with wind tunnel tests and comprehensive analysis — Bo105 hingeless rotor

Figures 7-10 present comparisons between predictions made with the developed aeroelastic rotor model (Sim) and wind tunnel (WT) measurements of oscillatory structural blade loads for the hingeless rotor of the Bo105 helicopter. Results from simulations carried out with the non-real-time comprehensive rotorcraft code CAMRAD/JA (CMRD/JA) are also included for comparison. All measured data as well as CAMRAD/JA predictions were extracted from Ref. 48. For the predictions presented in this section, the main rotor was numerically trimmed in terms of prescribed non-dimensional thrust ($C_t = \frac{T}{\rho\pi\Omega^2 R^4}$) and hub moments ($C_{L,M} = \frac{L,M}{\rho\pi\Omega^2 R^5}$) where T, L, and M are the rotor thrust, rolling, and pitching moment respectively. This was done in order to match the operating conditions of each test case as described in Ref. 48 and summarised in Table 3.

The results presented in Figs 7 and 8 correspond to an advance ratio of $\mu = 0{\cdot}197$ and a shaft angle of $a = -4{\cdot}8^\circ$ relative to the free-stream flow, whilst Figs 9 and 10 show comparisons for $\mu = 0{\cdot}313$ and $a = -9{\cdot}6^\circ$. Comparisons of oscillatory flapwise and chordwise bending moments are presented for radial stations corresponding to the effective blade root ($r/R = 0{\cdot}144$) and near mid-span ($r/R = 0{\cdot}57$) locations. Oscillatory torsional moments are presented for radial stations located near mid-span at $r/R = 0{\cdot}40$ and $r/R = 0{\cdot}57$, respectively.

Figures 7(a) and 8(a) present comparisons between predictions and wind tunnel measure ments

https://doi.org/10.1017/S0001924000010496 Published online by Cambridge University Press

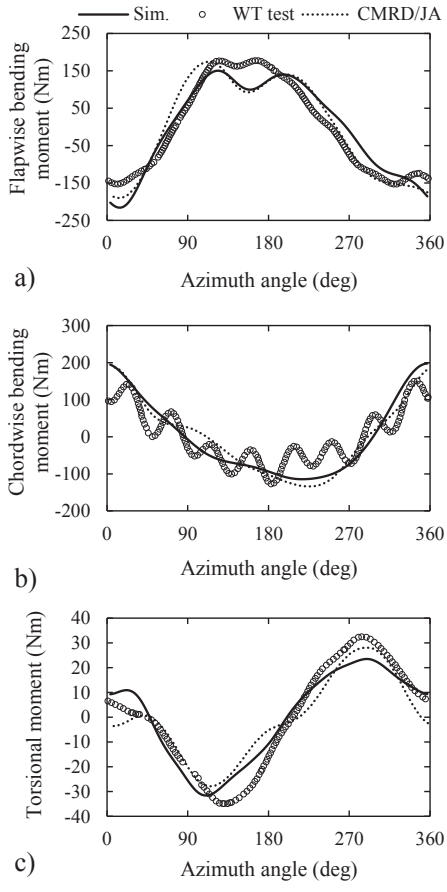


Figure 7. Oscillatory blade loads for the hingeless rotor of the Bo 105 helicopter, $\mu = 0{\cdot}197$ – Comparison with wind tunnel experiments and CAMRAD/JA simulations from Ref. 48: (a) Flapwise bending moment for $r/R = 0{\cdot}144$, (b) Chordwise bending moment for $r/R = 0{\cdot}144$, (c) Torsional moment for $r/R = 0{\cdot}40$.

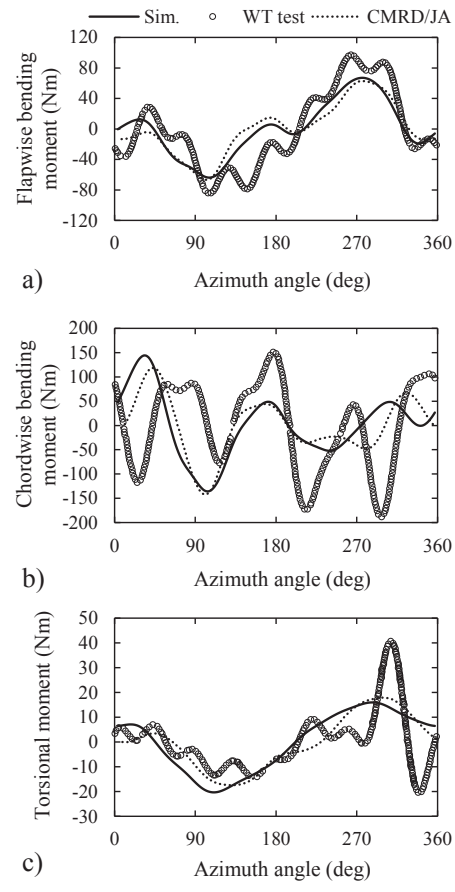


Figure 8. Oscillatory blade loads for the hingeless rotor of the Bo 105 helicopter, $\mu = 0{\cdot}197$ – Comparison with wind tunnel experiments and CAMRAD/JA simulations from Ref. 48: (a) Flapwise bending moment for r/R = 0·57, (b) Chordwise bending moment for $r/R = 0{\cdot}57$, (c) Torsional moment for $r/R = 0{\cdot}57$.

CAMRAD/JA simulations of oscillatory flapwise blade bending moment for $\mu = 0{\cdot}197$. Good agreement is observed between results obtained from simulations carried out with both rotor models. Figure 7(a) demonstrates that for $r/R = 0{\cdot}144$, the agreement between the present numerical approach and experimental data considering the 1P component of flap bending moment at the blade root is very good. This is due to the fact that, the quasi-steady hub moments were essentially prescribed by the trim procedure. It is noted that CAMRAD/JA as well as the model presented in this paper, both overpredicted the 2P and 3P components of oscillatory loading compared to the wind tunnel measurements. Figure 8(a) shows that for $r/R = 0{\cdot}57$, the present approach agrees well with CAMRAD/JA in terms of capturing the basic waveform of the measured test results. Both models succeeded in capturing the amplitude of the 3P moment component but underpredicted the impact of 2P loading. Neither model succeeded in predicting the 8P oscillatory component of flap moment as measured in the wind tunnel.

https://doi.org/10.1017/S0001924000010496 Published online by Cambridge University Press

Figures 7(b) and 8(b) present the corresponding comparisons for the oscillatory components of chordwise bending moment. Figure 7(b) shows that with respect to the effective blade root location (r/R = 0·144), both simulation models succeeded in capturing the basic waveform of chordwise loading. Neither CAMRAD/JA, nor the present model were able to predict the 8P oscillatory component as measured in the wind tunnel. Figure 8(b) shows that for the near mid-span location (r/R = 0·57), neither CAMRAD/JA nor the present model succeeded in capturing the qualitative nature of chordwise loading. However, very good agreement is demonstrated between CAMRAD/JA and the modelling approach of this paper. This is a strong indication that, both rotor models essentially exhibit similar levels of accuracy for prediction of oscillatory blade loads. This observation is valid considering higher values of advance ratio where the influence of the wake roll-up on induced flow is substantially reduced.

It is noted that, according to Ref. 48, significant aerodynamic interaction effects were present between the main rotor and the test apparatus during the wind tunnel experiments. This aerodynamic interaction, which was not modeled by neither numerical approach, essentially resulted in high-frequency harmonic content in the measured data. It is believed that, the significant discrepancies observed in Fig. 8(b) between the wind tunnel test results and the predictions made with both rotor codes, are largely due to these unmodeled interaction effects. This high-frequency content in the wind tunnel data is evident throughout the comparisons presented in this paper.

Figures 7(c) and 8(c) present comparisons of oscillatory torsional moment for μ = 0·197. Good agreement is exhibited in Fig. 7(c) for r/R = 0·40 between predictions made with both simulation models and wind tunnel measurements. A similar prediction of oscillatory loading behaviour is observed in Fig. 8(c) for r/R = 0·57. It can be noticed that, the 8P moment component present in the wind tunnel data for r/R = 0·57 was not captured neither by neither simulation model. Good agreement can be observed between predictions made with the present modelling approach and CAMRAD/JA for both radial stations. The present formulation underpredicted slightly the oscillatory magnitude of 3P and 4P loading components relative to the CAMRAD/JA results.

Figures 9(a) and 10(a) compare predictions of oscillatory flapwise bending moment with wind tunnel measurements and CAMRAD/JA simulations for μ = 0·313. Figure 9(a) demonstrates that for r/R = 0·144, the present modelling approach agrees well, both with CAMRAD/JA as well as with wind tunnel measurements concerning the 1P component of flap moment. Better agreement is noted between the present formulation and the wind tunnel data as regards the 2P component of oscillatory loading, compared to the predictions made with CAMRAD/JA. Both simulation models overpredicted the amplitude of the 3P component of flap bending moment. Figure 10(a) shows that for r/R = 0·57, the employed modelling approach agrees very well with CAMRAD/JA. Both numerical formulations captured the basic waveform of the measured test results, although they underpredicted the magnitude of 1P and 2P loading compared to the measured data.

Figures 9(b) and 10(b) present the respective comparisons for the oscillatory components of chordwise bending moment. Figure 9(b) shows that, considering the effective blade root location (r/R = 0·144), the agreement between predictions made with the presentud rotor model and wind tunnel measured data is very good. The proposed numerical formulation captured successfully the behaviour of 1P and 2P oscillatory moment components as measured in the wind tunnel. CAMRAD/JA did not succeed in accurately predicting either component of chordwise loading as reported in the test data. Figure 10(b) demonstrates that, near the blade mid-span location (r/R = 0·57), although there is good agreement between both simulation models, the agreement between model predictions and wind tunnel test results is relatively poor. This essentially constitutes another indication that, both simulation models exhibit similar levels of modelling accuracy and inadvertently face similar limitations in the context of loads prediction. The discrepancies noted between

https://doi.org/10.1017/S0001924000010496 Published online by Cambridge University Press

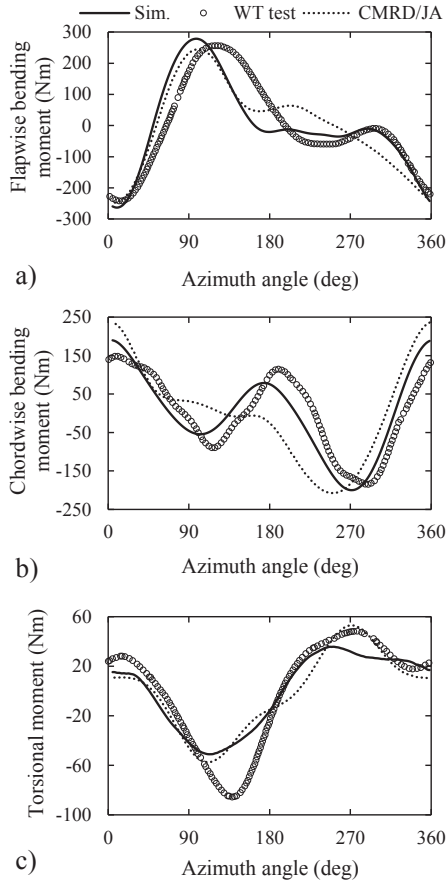


Figure 9. Oscillatory blade loads for the hingeless rotor of the Bo 105 helicopter, $\mu = 0{\cdot}313$ – Comparison with wind tunnel experiments and CAMRAD/JA simulations from Ref. 48: (a) Flapwise bending moment for $r/R = 0{\cdot}144$, (b) Chordwise bending moment for $r/R = 0{\cdot}144$, (c) Torsional moment for $r/R = 0{\cdot}40$.

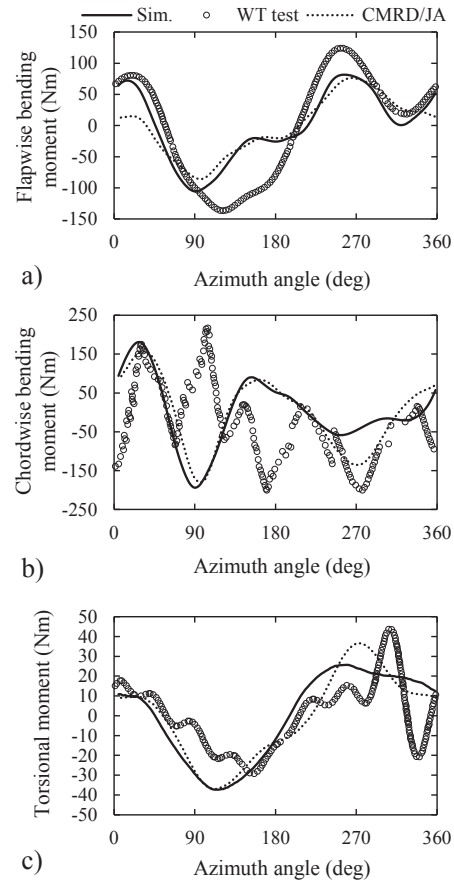


Figure 10. Oscillatory blade loads for the hingeless rotor of the Bo 105 helicopter, $\mu = 0{\cdot}313$ – Comparison with wind tunnel experiments and CAMRAD/JA simulations from Ref. 48: (a) Flapwise bending moment for $r/R = 0{\cdot}57$, (b) Chordwise bending moment for $r/R = 0{\cdot}57$, (c) Torsional moment for $r/R = 0{\cdot}57$.

model predictions and measured data are largely attributed to the aforementioned aerodynamic interaction effects between the main rotor and the test apparatus.

Figures 9(c) and 10(c) present comparisons of oscillatory torsional moment for the same trim conditions. Good agreement is observed in Fig. 9(c) between predictions made with the present model and CAMRAD/JA for $r/R = 0{\cdot}4$. Agreement is best for the 1P and 2P components of oscillatory loading. CAMRAD/JA however predicted higher amplitude for the 3P moment component compared to the simulations performed with the present numerical approach. Although good agreement with measured data is observed for both simulation models, they both also underpredicted the amplitude of the 2P component of torsional moment. Figure 10(c) demonstrates good agreement between predictions carried out with the two rotor models for $r/R = 0{\cdot}57$ considering the 1P and 2P components of oscillatory loading. However, both models overpredicted the impact of 1P loading compared to the wind tunnel data. CAMRAD/JA predicted higher amplitude for

https://doi.org/10.1017/S0001924000010496 Published online by Cambridge University Press

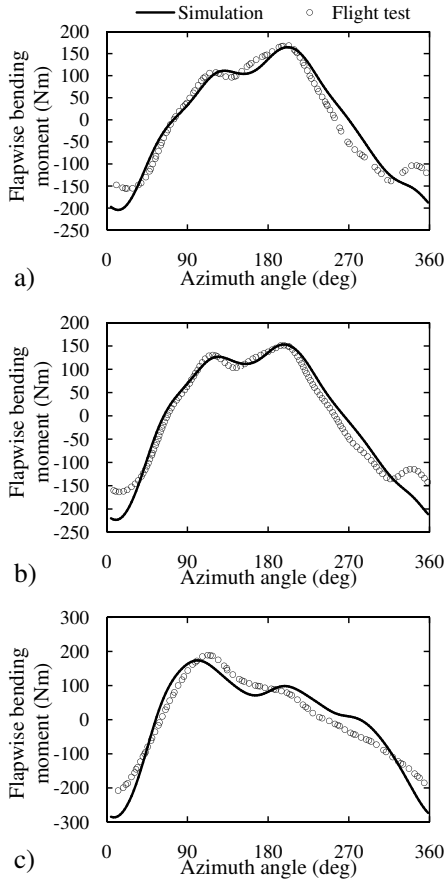


Figure 11. Oscillatory flapwise blade bending moment for the hingeless rotor of the Bo105 helicopter, r/R = 0·144 – Comparison with flight test data from Ref. 48: (a) μ = 0·197, (b) μ = 0·225 (c) μ = 0·306.

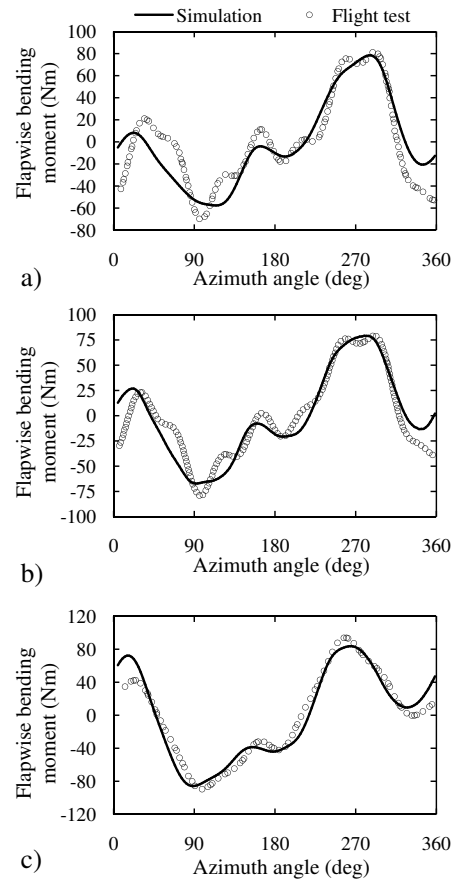


Figure 12. Oscillatory flapwise blade bending moment for the hingeless rotor of the Bo105 helicopter, r/R = 0·57 – Comparison with flight test data from Ref. 48: (a) μ = 0·197, (b) μ = 0·225 (c) μ = 0·306.

the 3P moment component relative to the present numerical approach and the test data. Neither simulation model captured the higher frequency 8P harmonic content as measured in the wind tunnel.

It was therefore shown that, the aeroelastic rotor model of this paper and the non-real-time comprehensive code CAMRAD/JA, essentially exhibit similar levels of accuracy considering the prediction of oscillatory blade loads. The two models performed along similar lines due to the fact that, they both account for the dominant dynamic and aerodynamic effects that influence rotor performance and loads. The absence of elastic coupling and wake roll-up effects in the simulations reported in this paper, does not seem to have affected the overall model accuracy. However, it is noted that the presented comparisons were carried out for $\mu \geq 0{\cdot}1$, where the wake is quickly swept away from the rotor by the free-stream flow and the roll-up effect is diminished. Thus, it can be concluded that the proposed aeroelastic rotor model can be successfully deployed for the estimation of oscillatory blade loads, considering flight regimes where the wake roll-up effect on induced flow is relatively weak and the assumption of a skewed cylindrical wake is valid (typically $\mu \geq 0{\cdot}1$).

https://doi.org/10.1017/S0001924000010496 Published online by Cambridge University Press

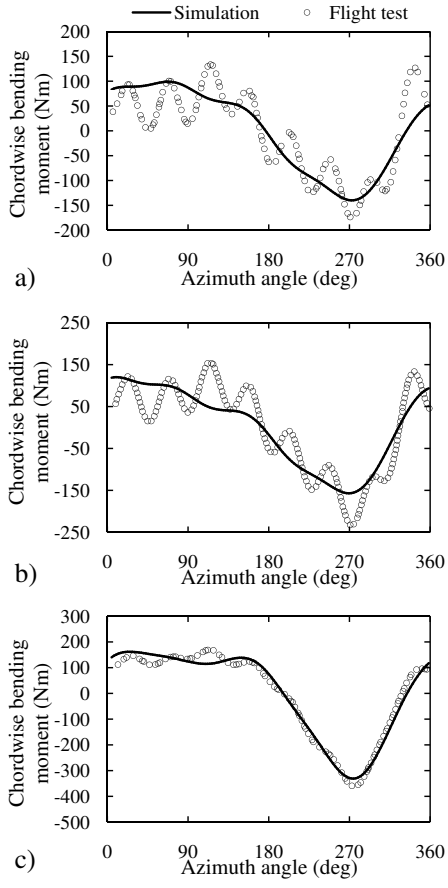


Figure 13. Oscillatory chordwise blade bending moment for the hingeless rotor of the Bo105 helicopter, r/R = 0·144 – Comparison with flight test data from Ref. 48: (a) μ = 0·197, (b) μ = 0·225 (c) μ = 0·306.

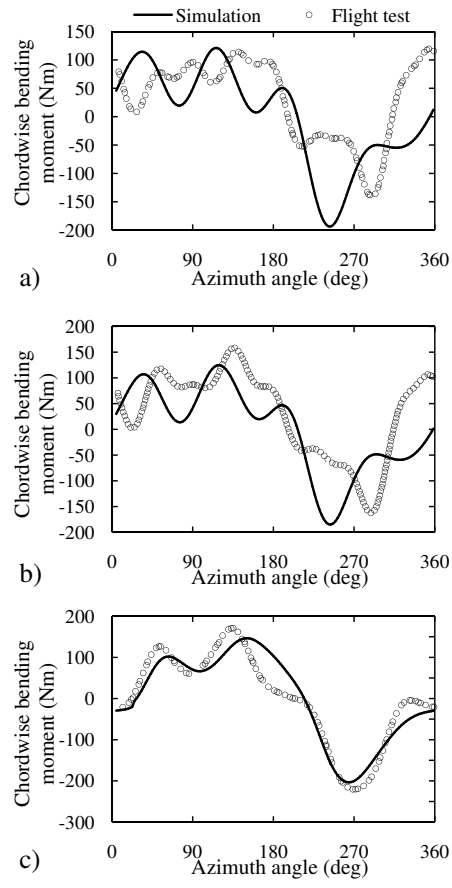


Figure 14. Oscillatory chordwise blade bending moment for the hingeless rotor of the Bo105 helicopter, – r/R = 0·45 – Comparison with flight test data from Ref. 48: (a) μ = 0·197, (b) μ = 0·225 (c) μ = 0·306.

3.3.2 Comparison with flight tests — Bo105 hingeless rotor

Figures 11-15 present comparisons of oscillatory structural blade loads, between predictions made with the developed aeroelastic rotor model and flight test data for the hingeless rotor of the Bo105 helicopter. Results are presented for straight and level flight at three values of advance ratio; μ = 0·197, μ = 0·225 and μ = 0·306. The corresponding rotor trim conditions are summarised in Table 3. The presented flight test data were extracted from Ref. 48. Comparisons of flapwise and chordwise bending moments were carried out at different mid-span radial locations in order to maintain consistency with the available measurements. Flapwise bending moment results near mid-span correspond to r/R = 0·57 while oscillatory chordwise loading is presented for r/R = 0·45. Both flap and chord bending moment predictions at the blade root were extracted for r/R = 0·144. Comparisons of torsional moments are only presented for one radial location corresponding to r/R = 0·40. Comparisons with CAMRAD/JA are not presented in this section due to lack of available simulation data with respect to the specific flight test conditions.

https://doi.org/10.1017/S0001924000010496 Published online by Cambridge University Press

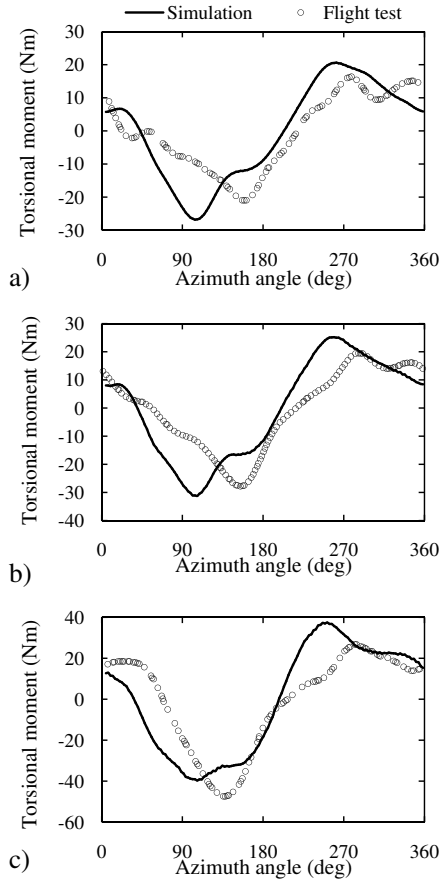


Figure 15. Oscillatory torsional blade moment for the hingeless rotor of the Bo105 helicopter, – r/R = 0·40 – Comparison with flight test data from Ref. 48: (a) μ = 0·197, (b) μ = 0·225 (c) μ = 0·306.

Figures 11 and 12 present comparisons of oscillatory flapwise blade bending moment between predictions made with the described aeroelastic rotor model and flight test data. Results are presented for the effective blade root (r/R = 0·144) and near mid-span (r/R = 0·57) radial stations in Figs 11 and 12 respectively.

Good agreement is exhibited with respect to the oscillatory component of flapwise loading at the effective blade root location (Fig. 11) for all values of advance ratio. The 1P loading component was accurately captured in terms of both amplitude and phase. This is due to the fact that, rotor trim was performed for prescribed thrust and hub moment settings. The comparisons suggest that, the 2P and 3P oscillatory components of flap bending moment are slightly over and underpredicted respectively. It is however noted that, the loading waveform shapes were fairly well captured for all flight conditions investigated, although agreement is best for μ = 0·197 and μ = 0·225.

Good agreement of oscillatory flap moment between predictions and flight test measurements, can also be observed for the near mid-span blade location in Fig. 12. The 1P component of loading was fairly accurately captured for all advance ratios. Good agreement is also noted with respect to the 2P and 3P components of oscillatory flapwise bending moment. The higher frequency 8P

https://doi.org/10.1017/S0001924000010496 Published online by Cambridge University Press

harmonic content observed in the flight test data for $\mu = 0{\cdot}197$ and $\mu = 0{\cdot}225$, was not predicted by the present modelling approach.

Figures 13-14 present comparisons of oscillatory chordwise blade bending moment, between predictions made with the present aeroelastic rotor formulation and flight test data. Results are presented for the effective blade root ($r/R = 0{\cdot}144$) and near mid-span ($r/R = 0{\cdot}45$) radial stations in Figs 13 and 14 respectively.

Figure 13 shows that, the basic waveform shape of chordwise bending moment at the blade root ($r/R = 0{\cdot}144$) has been adequately captured for all advance ratios. The components of chordwise moment were accurately predicted in terms of both amplitude and phase angle, up to the third harmonic (3P) of oscillatory loading. It is however noted that, higher frequency content reaching up to the eighth harmonic of loading (8P) is present in the flight test data. This high-frequency loading tends to decrease with increasing advance ratio and was not captured by the analysis.

With respect to the radial location corresponding to $r/R = 0{\cdot}45$, Fig. 14 shows good agreement between simulation and flight test data considering the 1P component of oscillatory chordwise loading. However, the agreement regarding higher harmonic content is poor in terms of both amplitude and phase for the comparisons performed for $\mu = 0{\cdot}197$ and $\mu = 0{\cdot}225$. Better agreement is observed for $\mu = 0{\cdot}306$ with respect to both 2P and 3P harmonic components of oscillatory loading.

Figure 15 presents comparisons of oscillatory torsional blade moment for $r/R = 0{\cdot}40$, between predictions made with the present aeroelastic rotor model and flight test data. Good agreement can be noted for all advance ratios. It can be observed that, torsional moment at the particular radial location comprises predominantly 1P harmonic content. This content was accurately predicted in terms of amplitude. However, there is an underprediction in the phase angle of 1P loading which reaches approximately 20º. This effectively leads to the appearance of peak loads at lower azimuth angles in comparison to the measured data. It is noted that, this difference in phase angle occurs relative to the wind tunnel data as well. This was attributed in Ref. 48 to the different torsional stiffness of the pitch control system incorporated by the Bo105 helicopter rotor that was deployed for the flight test measurements. This difference in torsional stiffness may have affected the blade's natural frequencies for torsional vibration leading to different phase angles in the torsion response. It can also be observed that, higher harmonic content (2P and 3P loading) is of relatively low amplitude for $\mu = 0{\cdot}197$ but increases substantially with increasing advance ratio.

3.3.3 Comparison with flight tests and comprehensive analysis — SA330 articulated rotor

Figures 16-19 present comparisons between predictions made with the developed aeroelastic rotor model (Sim) and flight test data (FT) of oscillatory blade structural loads for the full-scale articulated rotor of the SA330 helicopter. Results from simulations carried out with the comprehensive rotorcraft code CAMRAD/JA (CMRD/JA) are also compared with the present modelling approach. Results are presented for $\mu = 0{\cdot}307$ and $\mu = 0{\cdot}321$. In contrast to the Bo105 helicopter test case where the main rotor is numerically trimmed to produce prescribed values of thrust and hub moments, the simulations presented in this section correspond to complete aircraft trim solutions. Comparisons of flapwise bending moment are presented for two blade radial locations corresponding to $r/R = 0{\cdot}35$ and $r/R = 0{\cdot}55$ respectively. Chordwise bending moment comparisons are presented for $r/R = 0{\cdot}73$. Comparisons of torsional blade moment correspond to $r/R = 0{\cdot}33$. The flight test data as well as CAMRAD/JA simulation results were extracted from from Ref. 46.

Figures 16 and 17 present comparisons between simulations and measurements of oscillatory flapwise blade bending moment for $r/R = 0{\cdot}35$ and $r/R = 0{\cdot}55$ respectively. Results are presented for $\mu = 0{\cdot}307$ Figs 16(a) and 16(a) and $\mu = 0{\cdot}321$ Figs 17(b) and 17(b). Comparisons with CAMRAD/

https://doi.org/10.1017/S0001924000010496 Published online by Cambridge University Press

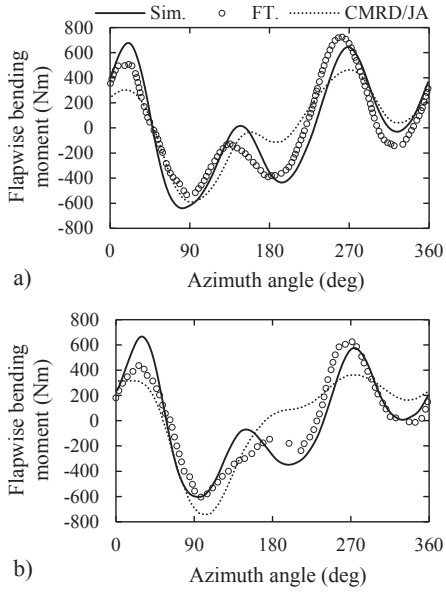


Figure 16. Oscillatory flapwise blade bending moment for the articulated rotor of the SA330 helicopter, r/R = 0·55 – Comparison with flight test data and CAMRAD/JA simulations from Ref. 46: (a) μ = 0·307, (b) μ = 0·321.

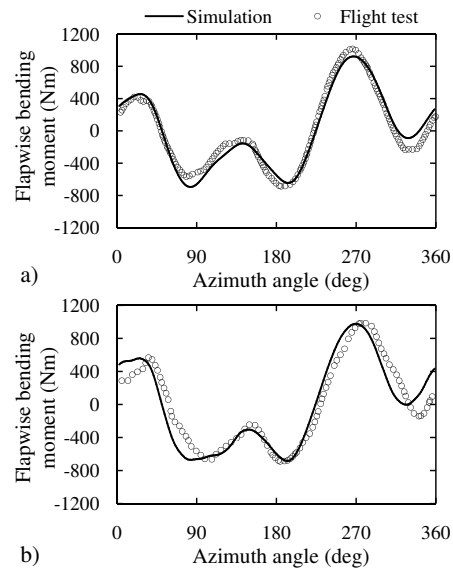


Figure 17. Oscillatory flapwise blade bending moment for the articulated rotor of the SA330 helicopter, r/R = 0·55 – Comparison with flight test data from Ref. 46: (a) μ = 0·307, (b) μ = 0·321.

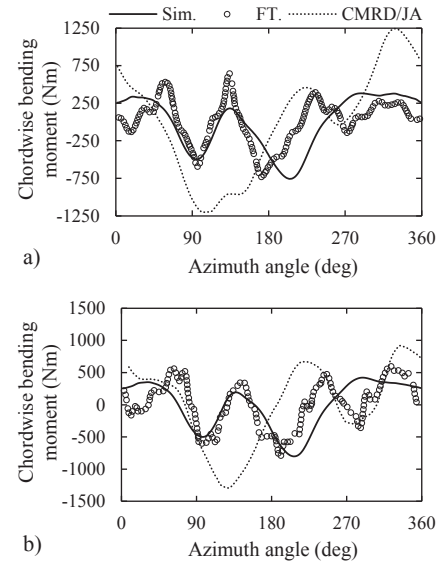


Figure 18. Oscillatory chordwise blade bending moment for the articulated rotor of the SA 330 helicopter, r/R = 0·73 – Comparison with flight test data and CAMRAD/JA simulations from Ref. 46: (a) μ = 0·307, (b) μ = 0·321.

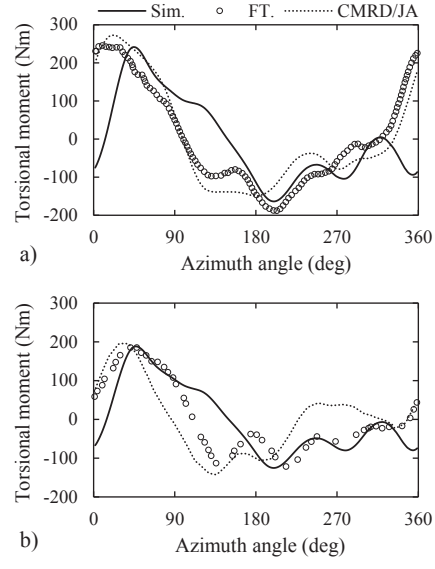


Figure 19. Oscillatory torsional blade moment for the articulated rotor of the SA 330 helicopter, r/R = 0·33 – Comparison with flight test data and CAMRAD/JA simulations from Ref. 46: (a) μ = 0·307, (b) μ = 0·321.

https://doi.org/10.1017/S0001924000010496 Published online by Cambridge University Press

JA are only carried out for $r/R = 0{\cdot}35$ due to lack of available data in Ref. 46. It can be noticed that, oscillatory flapwise loading comprises predominantly 1P and 3P harmonic content considering both radial locations and both values of advance ratio. Good agreement can generally be observed between both simulation models and flight test data. It is evident that the nature of the fundamental 1P loading was adequately captured by the proposed modelling approach. It is emphasised that this was achieved without the prescription of designated rotor hub moments. With respect to higher harmonic content, it can be noted that the present model was able to predict accurately the nature of 3P oscillatory loading, both in terms of amplitude and phase. The amplitude of 2P harmonic content appears to be slightly underpredicted compared to the measured data. CAMRAD/JA was successful in capturing the amplitude of 2P loading but underpredicted significantly the dominant nature of 3P oscillatory moment. As such, the flapwise loading waveforms predicted by CAMRAD/JA appear to deviate substantially from the measured data in Fig. 16.

Figures 18(a) and 18(b) present comparisons between predictions and flight test measurements of oscillatory chordwise bending moment for $\mu = 0{\cdot}307$ and $\mu = 0{\cdot}321$ respectively. The presented results correspond to the radial station located at $r/R = 0{\cdot}73$. The agreement between predictions carried out with the present rotor model and the measured data, can only be described as fair in the sense that the overall amplitude of oscillatory loading was captured. The measurements suggest that chordwise loading consists primarily of 4P harmonic content. There are also contributing components of 1P, 2P, 3P, and 5P loading but they are significantly smaller in terms of amplitude. Both CAMRAD/JA as well as the simulation model of this paper, predict significantly larger amplitude for the respective low-frequency harmonic components (1P-3P) compared to the measured data. The higher harmonic content residing in the measured waveforms was not captured by neither model. The larger discrepancies observed between model predictions and flight test data compared to the flap bending case, are attributed to inaccurate aerofoil data with respect to drag coefficients.

Figures 19(a) and 19(b) present comparisons between model predictions and measurements of oscillatory torsional blade moment for $\mu = 0{\cdot}307$ and $\mu = 0{\cdot}321$, respectively. Comparisons were carried out for $r/R = 0{\cdot}33$. Good agreement can be observed between predictions performed with the present modelling approach and flight test data for both values of advance ratio. The lower-frequency harmonic content (1P-3P) of oscillatory loading was fairly accurately captured in terms of amplitude. However, the phase angle of 1P loading was underpredicted by approximately 30º for $\mu = 0{\cdot}307$. This is attributed to inaccurate aerofoil data in terms of pitching moment coefficients. It is emphasised at this point that, a two-dimensional, compressible, potential-flow panel method coupled with a linearised viscous boundary layer solution[49], was used for the derivation of cross-sectional aerodynamic characteristics employed for modelling the SA330 rotor blades. Thus, potential modelling uncertainties associated with the implicit assumptions of the aforementioned approach, essentially propagated and inevitably compromised the accuracy of the obtained solution. CAMRAD/JA, which essentially employed measured data for the blade's cross-sectional aerodynamics, was successful in capturing the phase angle of 1P loading for $\mu = 0{\cdot}307$. The higher frequency harmonic content residing in the measured waveforms, was not predicted by neither simulation model. Agreement between predictions and flight test data is best for $\mu = 0{\cdot}321$.

3.4 Rotor blade vibratory flap bending moment

Figures 20-22 present comparisons between predictions and wind tunnel/flight test measurements of the vibratory components of flapwise bending moment at the effective blade root location considering both helicopter configurations. A harmonic analysis was carried out on the measured and predicted waveforms of oscillatory flap loading at the blade root. Only the harmonic components capable of transmitting vibratory loads to the fuselage were retained. According to Ref. 42, for

https://doi.org/10.1017/S0001924000010496 Published online by Cambridge University Press

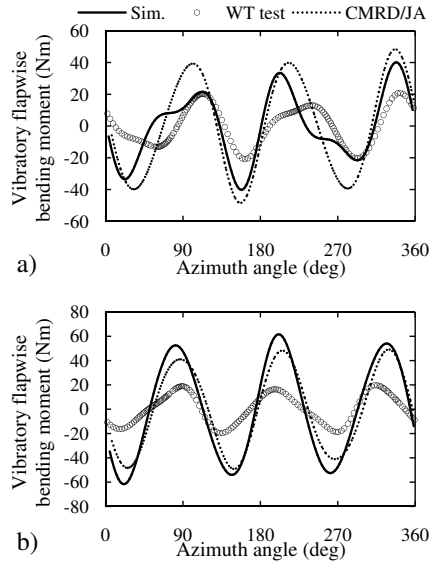


Figure 20. Vibratory flapwise bending moment for the hingeless rotor of the Bo 105 helicopter, r/R = 0·144 – Comparison with flight test data and CAMRAD/JA simulations from Ref. 48: (a) μ = 0·197, (b) μ = 0·313.

perfectly matched blades, the condition for retaining the kth harmonic of oscillatory flap moment in the calculated vibratory flap loading waveform can be expressed as:

$$k = m \cdot N_b \pm 1, \quad m = 1,2,3\ldots \qquad \ldots (65)$$

The harmonics not complying with the condition expressed by Equation (65), were discarded from the reconstructed waveforms presented in Figs 20-22.

Figure 20 presents comparisons between predictions and wind-tunnel measurements — CAMRAD/JA simulations of vibratory flap loading at the effective blade root location (r/R = 0·144) for the Bo105 hingeless rotor. Results are presented for μ = 0·197 and μ = 0·313 in Figs 20, (a) and 20, (b) respectively. It can be observed that, the vibratory flap moment as measured in the wind tunnel comprises predominantly 3P and 5P oscillatory loading. The effect of higher harmonic content is negligible. The effect of 5P loading is more pronounced for μ = 0·197. CAMRAD/JA failed to capture the influence of 5P loading considering both advance ratios. The developed rotor model predicted moderate 5P loading for μ = 0·197 but the phase correlation with the wind tunnel data is poor. Good agreement in terms of amplitude and phase is observed between both simulation models for μ = 0·313. The correlation with wind tunnel data is excellent in terms of phase but poor in terms of amplitude considering both simulation models.

Figure 21 presents comparisons of vibratory flap bending moment between predictions made with the described aeroelastic rotor model and flight test data for the Bo105 hingeless rotor. Comparisons are shown for μ = 0·197, μ = 0·225 and μ = 0·306 in Figs 21 (a) (b) and (c), respectively. Results are presented for the effective blade root radial station (r/R = 0·144). It is observed that, similarly to the tests conducted in the wind tunnel, the measured vibratory flap moment comprises predominantly 3P and 5P oscillatory loading. The 3P component of vibratory loading was fairly well captured by the developed numerical approach, both in terms of amplitude and phase considering all values of advance ratio. The amplitude of the 5P component was adequately predicted but the phase angle

https://doi.org/10.1017/S0001924000010496 Published online by Cambridge University Press

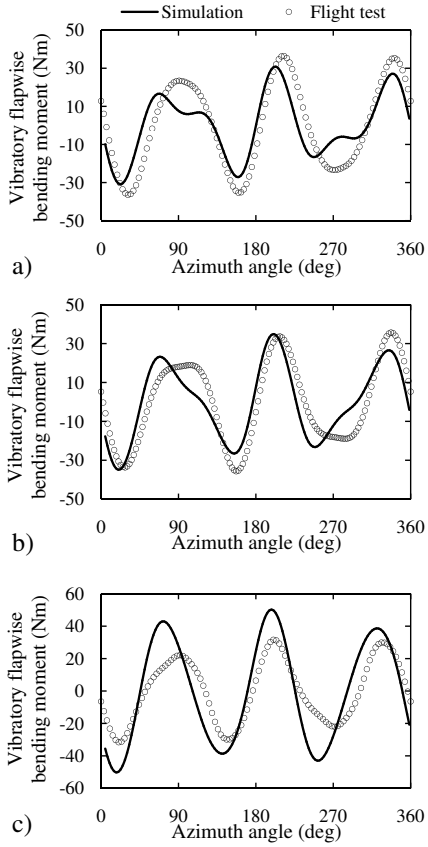


Figure 21. Vibratory flapwise bending moment for the hingeless rotor of the Bo105 helicopter, r/R = 0·144 – Comparison with flight test data from Ref. 48: (a) μ = 0·197, (b) μ = 0·225 (c) μ = 0·306.

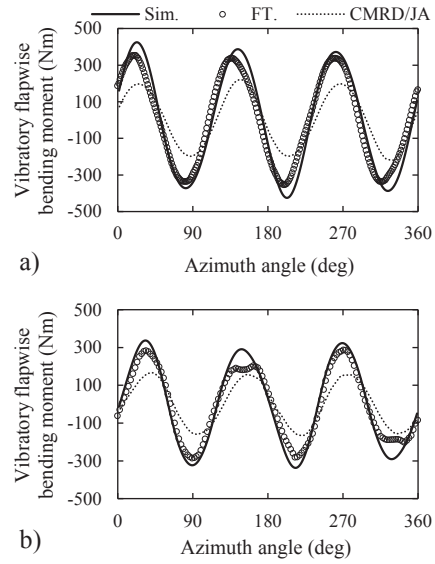


Figure 22. Vibratory flapwise bending moment for the articulated rotor of the SA330 helicopter, r/R = 0·35 Comparison with flight test and CAMRAD/JA simulations data from Ref. 46: (a) μ = 0·307, (b) μ = 0·321.

correlation with flight test data is poor. Furthermore, the simulations predicted gradually decreasing amplitude for the 5P harmonic component with increasing advance ratio.

Figure 22 presents comparisons of vibratory flap bending moment between predictions made with the present modelling approach and flight test data for the SA330 articulated rotor. Comparisons are shown for μ = 0·307 and μ = 0·321. Results from simulations carried out with CAMRAD/JA (CMRD/JA) are also compared with the aeroelastic rotor model of this paper. Comparisons are presented for r/R = 0·35, since this is the radial location closer to the rotor hub for which measured data is available in Ref. 46. Very good agreement in terms of amplitude and phase is observed between simulations and flight test measurements. Both predicted as well as measured vibratory waveforms consist predominantly of 3P oscillatory loading. The influence of higher harmonic content in the measured data is negligible for μ = 0·307 but becomes noticeable for μ = 0·321. CAMRAD/JA underpredicts considerably the amplitude of 3P vibratory flap bending moment at the rotor hub considering both values of advance ratio. The subtle effect of higher harmonic content for μ = 0·321 was not captured by neither simulation model.

https://doi.org/10.1017/S0001924000010496 Published online by Cambridge University Press

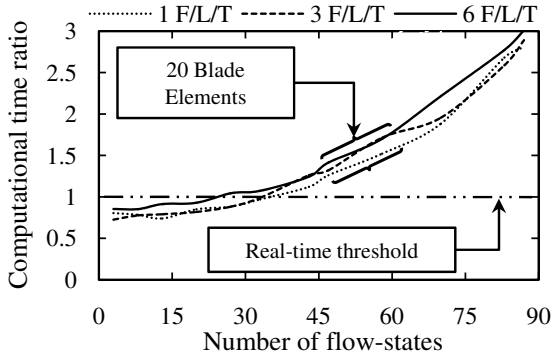


Figure 23. Influence of number of flow-states and flap-lag-torsion modes (F-L-T) on the computational time ratio for a personal computer with a 2·3GHz CPU and 4GB of RAM.

3.5 Assessment of computational time requirements

In order to evaluate the suitability of the proposed numerical approach for real-time aeromechanics applications, the computational time requirements associated with nonlinear aeroelasticity analysis were thoroughly assessed. An effective parameter is defined, namely the computational time ratio (R_{comp}), as the total computational time required (T_{req}) per simulated time of unsteady rotor operation (T_{sim}). The simulated time of operation is given by $T_{sim} = N_{rev} \cdot \frac{2\pi}{\Omega}$, where Ω is the rotational speed of the shaft and N_{rev} is the number of simulated revolutions. The computational time ratio is given by $R_{comp} = \frac{T_{req}}{T_{sim}}$. Hence, for $R_{comp} \leq 1$ (real-time threshold) the model is able to predict the unsteady behaviour of the associated physical processes faster than they actually occur in nature. This allows for the proposed mathematical model to be deployed in real-time.

Figure 23 demonstrates the effect of number of flow-states and flap-lag-torsion (F-L-T) mode shapes on the computational time ratio. Results correspond to simulations performed for the hingeless rotor of the Bo105 helicopter and for 15 revolutions ($N_{rev} = 15$). Time measurements were conducted on a personal computer equipped with 4 gigabytes (GB) of random access memory (RAM) and a dual-core central processing unit (CPU) operating at 2·3 gigahertz (GHz). A total of 20 elements were used for the radial aerodynamic discretisation of each blade. A time-step of $\Delta t = 2 \cdot 10^{-3}$ sec was employed for time-marching leading to an equivalent azimuth-step of the order 5 degrees. The computational implementation of the mathematical model was carried out using FORTRAN 90 without the employment of parallel processing.

It is noticed that, the effect of number of F-L-T modes on the computational time ratio is relatively small. Computational times changed very slightly with the employment of up to six modes for each DOF. It is noted at this point that, inclusion of higher harmonic content in terms structural deformation modes is unlikely to improve agreement on oscillatory blade loads. This is due to the extremely high natural frequencies associated with higher-order modes which are unlikely to get excited by the external forcing, even at high-speed flight conditions. The influence of number of flow states on the computational time ratio was also investigated. Calculations were performed starting with three inflow states and were gradually increased up to ninety. The effect on computational effort is relatively small if one considers that computational time is almost

https://doi.org/10.1017/S0001924000010496 Published online by Cambridge University Press

tripled for increasing the number of flow-states by a factor of 30. However, it is noted that a total of 33-47 flow-states is sufficient for the majority of aeromechanics applications.

Figure 23 shows that for the typical personal computer used for the purpose of this work, real-time simulation is achievable using up to 33 flow-states and three F-L-T mode shapes. This effectively corresponds to an aeroelastic rotor model with sufficient fidelity for prediction of structural blade loads. The developed approach is expected to perform significantly faster on modern high-end machines used routinely in industry and academia, thus allowing for real-time simulation using model configurations with substantially higher fidelity. It can therefore be concluded that, the proposed mathematical model is indeed capable of execution in real-time aeroelasticity applications without the employment of parallel processing.

4.0 CONCLUSIONS

An integrated approach targeting the real-time simulation of aeroelastic rotor blade dynamics in helicopter aeromechanics applications was offered. A mathematical procedure applicable to the rapid estimation of natural vibration characteristics of helicopter rotor blades was developed. Lagrangian kinematics along with Bernoulli-Euler beam and classical torsional vibration theory, were utilised in order to derive an efficient numerical formulation applicable to rotating blades with nonuniform structural properties. A matrix/vector formulation was proposed for the treatment of three-dimensional elastic blade kinematics. In order to ensure robustness and establish applicability in real-time, a novel second-order accurate finite-difference algorithm was employed for the numerical discretisation of elastic blade motion in the time-domain. Integral expressions were derived for the time-dependent forces and moments exerted by the elastic blades on the rotor hub.

The described mathematical approach was numerically coupled with the Peters-He induced flow model, the Leishman-Beddoes blade element aerodynamics model and subsequently implemented in a helicopter flight mechanics simulation code. The aeroelastic behaviour of two full-scale helicopter rotors was investigated; the hingeless rotor of the MBB Bo105 and the articulated rotor of the A rospatiale SA330. Analyses were performed for rotor blade resonant frequencies, trim control angles, oscillatory structural blade loads and vibratory flap bending moment at the rotor hub. Extensive comparisons were carried out with measured data derived from wind tunnel experiments, flight tests and CAMRAD/JA simulations for a wide range of advance ratios. The computational requirements associated with execution of the proposed model were thoroughly assessed.

The general conclusions arising from the completion of this work can be summarised as follows:

- Good agreement was found between predictions made with the Lagrangian formulation and CAMRAD/Y-71 simulations with respect to flap-lag-torsion natural frequencies at nominal rotorspeed considering both helicopter rotor blade models.
- The developed flight mechanics model exhibited accurate predictive qualities with regards to rotor trim control angles and power requirement for straight and level flight considering both helicopter models. A small underprediction of lateral cyclic (θ_{1c}) was observed at very low advance ratios ($\mu \approx 0{\cdot}05$) which was attributed to the absence of rotor wake roll-up in the Peters-He induced flow model.
- The devised approach was successful in predicting the low-frequency components of oscillatory structural blade loads as measured in wind tunnel tests performed for the hingeless rotor of the Bo105 helicopter. The model was unable to adequately capture the higher frequency components (8P) of oscillatory loading.

https://doi.org/10.1017/S0001924000010496 Published online by Cambridge University Press

- The mathematical model of this paper and the comprehensive code CAMRAD/JA exhibit similar levels of accuracy for prediction of oscillatory blade loads. This conclusion is valid for advance ratios above $\mu \approx 0{\cdot}01$ where the wake roll-up effect on induced flow is diminished.
- Good agreement on oscillatory structural blade loads was observed between predictions made with the developed model and measurements derived from flight tests regarding both investigated helicopter configurations. Good agreement was found up to the 3P harmonic component of oscillatory loading.
- The developed mathematical approach was successful in predicting the 3P component of vibratory flap bending moment at the rotor hub in terms of magnitude and phase considering both helicopter rotor configurations. The model did not adequately capture the phase angle of the respective 5P oscillatory component residing in the vibratory measured waveforms.
- The overall methodology is suitable for real-time simulation without the use of parallel processing, employing sufficient modelling fidelity for accurate prediction of oscillatory blade loads.

It is thus understood that, the proposed numerical approach enables transition from classical rigid blade modelling to a complete framework for real-time aeroelasticity simulation without resorting to computationally expensive finite element analysis, multi-body dynamics, free-wake aerodynamics, or parallel processing. It is compatible with every rotor inflow and aerodynamic theory that can operate in the time-domain. It is readily available in compact form for implementation in existing aeromechanics codes without any change in the offered expressions. It is applicable to a wide-range of helicopter rotor configurations including hingeless, freely-hinged, and spring-hinged articulated rotors. It is suitable for rotor design due to its effective combination of high modelling fidelity and real-time applicability. As such, it constitutes an enabling technology for the implementation of flexible rotor blade dynamics in real-time helicopter aeromechanics applications such as; flight simulation, nonlinear control law design and automatic flight control system development.

REFERENCES

1. JOHNSON, W. *Rotorcraft Aeromechanics*, First ed, 2013, Cambridge University Press, Cambridge, UK.
2. JOHNSON, W. Milestones in rotorcraft aeromechanics, 2011, NASA Ames Research Center, TP-2011-215971.
3. PADFIELD, G.D. *Helicopter Flight Dynamics*, 2007, Blackwell Publishing, Oxford, UK.
4. HOWLETT, J.J. UH-60A Black Hawk engineering simulation program: **I**, Mathematical model, 1981, NASA, CR 166309.
5. SHUPE, N. A Study on the dynamic motions of hingeless rotored helicopters, 1970, US Army Electronics Command, TR ECOM-3323.
6. CURTISS, H. and SHUPE, N. A Stability and control theory for hingeless rotors, 1971, Proceedings of the 27th Annual Forum of the American Helicopter Society, May 1971, Washington, DC, USA.
7. BROWN, R.E. Rotor wake modelling for flight dynamic simulation of helicopters, *AIAA J*, January 2000, **38**, (1), pp 57-63.
8. JOHNSON, W. Rotorcraft aerodynamics models for a comprehensive analysis, Proceedings of the 54th Annual Forum of the American Helicopter Society, May 1998, Washington, DC, USA.
9. BROWN, R.E. and HOUSTON, S.S. Comparison of induced velocity models for helicopter flight mechanics, *J Aircr*, August 2000, **37**, (4), pp 623-629.
10. PITT., D.M. and PETERS, D.A. Theoretical prediction of dynamic inflow derivatives, *Vertica*, March 1981, **5**, (1), pp 21-34.
11. PETERS, D.A. and HAQUANG, N. Dynamic inflow for practical applications, *J American Helicopter Soc*, October 1988, **33**, (4), pp 64-68.

https://doi.org/10.1017/S0001924000010496 Published online by Cambridge University Press

12. THEODORE, C. and CELI, R. Helicopter flight dynamic simulation with refined aerodynamics and flexible blade modelling, 2000, 56th Annual Forum of the American Helicopter Society, 2-4 May 2000.
13. KIM, F.D., CELI, R. and TISCHLER, M.B. High-order state space simulation models of helicopter flight mechanics, *J American Helicopter Soc*, October 1993, **38**, (4), pp 16-27.
14. TURNOUR, S.R. and CELI, R. Modelling of flexible rotor blades for helicopter flight dynamics applications, *J American Helicopter Soc*, January 1996, **41**, (1), pp 52-66.
15. BAGAI, A. and LEISHMAN, J.G. Rotor free-wake modelling using a pseudo-implicit technique − including comparisons with experimental data, *J American Helicopter Soc*, April 1995, **40**, (3), pp 29-41.
16. LEWIS, W.D. An aeroelastic model structure investigation for a manned real-time rotorcraft simulation, 49th Annual Forum of the American Helicopter Society, May 1993, Saint Louis, MO, USA.
17. STURISKY, S.H. and SCHRAGE, D.P. System identification validation of an AH-64 aeroelastic simulation model, 1993, 49th Annual Forum of the American Helicopter Society, May 1993, Saint Louis, MO, USA.
18. YEO, H. and JOHNSON, W. Prediction of rotor structural loads with comprehensive analysis, *J American Helicopter Soc*, April 2008, **53**, (2), pp 193-209.
19. PIZIALI, R.A. and DUWALDT, F.A. A method for computing rotary wing airload distribution in forward flight, 1962, Cornell Aeronautical Laboratory, TCREC TR 62-44.
20. PIZIALI, R. and DUWALDT, F. Computed induced velocity, induced drag, and angle of attack distributions for a two-bladed rotor, 1963, 19th Annual Forum of the American Helicopter Society, May 1963, Washington, DC, USA.
21. PIZIALI, R., DAUGHADAY, H. and DUWALDT, F. Rotor airloads, 1963, CAL/TRECOM Symposium on Dynamic Load Problems Associated with Helicopters and V/STOL Aircraft, June 1963, Buffalo, NY, USA.
22. PIZIALI, R. A method for predicting the aerodynamic loads and dynamic response of rotor blades, January 1966, USAAVLABS, TR 65-74.
23. PIZIALI, R. Method for the solution of the aeroelastic response problem for rotating wings, *J Sound and Vibration*, November 1966, **4**, (3), pp 445-489.
24. YEO, H. and JOHNSON, W. Assessment of comprehensive analysis calculation of airloads on helicopter rotors, *J Aircr*, September 2005, **42**, (5), pp 1218-1228.
25. YEO, H. and JOHNSON, W. Comparison of rotor structural loads calculated using comprehensive analysis, 2005, 31st European Rotorcraft Forum, September 2005, Florence, Italy.
26. JOHNSON, W. Technology drivers in the development of CAMRAD II, 1994, American Helicopter Society Aeromechanics Specialists' Conference, January 1994, San Fransisco, CA, USA.
27. JOHNSON, W. General free wake geometry calculation for wings and rotors, 1995, 51st Annual Forum of the American Helicopter Society May 1995, Fort Worth, TX, USA.
28. JOHNSON, W. Rotorcraft dynamics models for a comprehensive analysis, 1998, 27th Annual Forum of the American Helicopter Society, May 1998, Washington, DC, USA.
29. PETERS, D.A., BOYD, D.D. and HE, C.J. Finite-state induced-flow model for rotors in hover and forward flight, *J American Helicopter Soc*, October 1989, **34**, (4), pp 5-17.
30. PETERS, D.A. AND HE, C.J. Correlation of measured induced velocities with a finite-state wake model, *J American Helicopter Soc*, July 1991, **36**, (3), pp 59-70.
31. VAN DER WALL, B.G., LIM, J.W., SMITH, M.J., JUNG, S.N., BAILLY, J., BAEDER, J.D. and BOYD, D.D. The HART II International Workshop: An assessment of the state-of-the-art in comprehensive code prediction, *CEAS Aeronaut J*, July 2013, **4**, (3), pp 223-252.
32. VAN DER WALL, B.G. A comprehensive rotary-wing database for code validation: The HART II International Workshop, *Aeronaut J*, February 2011, **115**, (1164), pp 91-102.
33. JOHNSON, W. A. History of rotorcraft comprehensive analyses, 2013, 69th Annual Forum of the American Helicopter Society, May 2013, Phoenix, AZ, USA.
34. JOHNSON, W. and DATTA, A. Requirements for next generation comprehensive analysis of rotorcraft, 2008, AHS Specialist's Conference on Aeromechanics, 23-25 January 2008, San Francisco, CA, USA.
35. VAN DER WALL, B.G. and ROTH, M. Free-wake analysis on massively parallel computers and validation with HART test data, 1997, 53rd Annual Forum of the American Helicopter Society, 29 April-1 May 1997, Virginia Beach, VA, USA.
36. HU, Q., GUMEROV, N.A., DURAISWAMI, R. and LEISHMAN, M.S.J.G. Toward improved aeromechanics simulations using recent advancements in scientific computing, 2011, 67th Annual Forum of the American Helicopter Society, 3-5 May 2011, Virginia Beach, VA, USA.
37. BHAGWAT, M.J. and LEISHMAN, J.G. Stability, consistency and convergence of time-marching free-vortex rotor wake algorithms, *J American Helicopter Soc*, January 2001, **46**, (1), pp 59-71.

https://doi.org/10.1017/S0001924000010496 Published online by Cambridge University Press

38. JOHNSON, W. CAMRAD/JA, *A Comprehensive Analytical Model of Rotorcraft Aerodynamics and Dynamics Vol I: Theory Manual*, 1988, Johnson Aeronautics, Palo Alto, CA, USA.
39. JOHNSON, W. *A Comprehensive Analytical Model of Rotorcraft Aerodynamics and Dynamics Vol II: User Manual*, 1988, Johnson Aeronautics, Palo Alto, CA, USA.
40. BISPLINGHOFF, R.L., ASHLEY, H. and HALFMAN, R.L. *Aeroelasticity*, 1996, Dover Publications, Mineola, New York, NY, USA.
41. GOULOS, I., PACHIDIS, V. and PILIDIS, P. Lagrangian formulation for the rapid estimation of helicopter rotor blade vibration characteristics, *Aeronaut J*, August 2014, **118**, (1206).
42. BRAMWELL, A.R.S. DONE, G. and BALMFORD, D. *Bramwell's Helicopter Dynamics*, 2001, Butterworth-Heinemann, Oxford, UK.
43. LEISHMAN, J.G. AND BEDDOES, T.S. A semi-empirical model for dynamic stall, *J American Helicopter Soc*, July 1989, **34**, (3), pp 3-17.
44. NOONAN, K.W. AND BINGHAM, G.J. Two-dimensional aerodynamic characteristics of several rotorcraft aerofoils at Mach numbers from 0·35 to 0·90 January 1977, NASA Langley Research Center, TM X-73990.
45. STALEY, J.A. Validation of rotorcraft flight simulation program through correlation with flight data for soft-in-plane hingeless rotor, 1976, USAAMRDL-TR-75-50.
46. BOUSMAN, W.G., YOUNG, C., TOULMAY, F., GILBERT, N.E., STRAWN, R.C., MILLER, J.V., COSTES, T.H.M.M. and BEAUMIER, P. A Comparison of lifting-line and CFD methods with flight test data from a research Puma helicopter, 1996, NASA, TM-110421.
47. PADFIELD, G.D., BASSET, P.M., DEQUIN, A.M., VON GRUNHAGEN, W., HADDON, D., HAVERDINGS, H., KAMPA, K. and MCCALLUM, A.T. Predicting rotorcraft flying qualities through simulation modelling. A review of key results from Garteur AG06, September 1996, 22nd European Rotorcraft Forum, Brighton, UK.
48. PETERSON, R.L., MAIER, T., LANGER, H.J. and TRANAPP, N. Correlation of wind tunnel and flight test results of a full-scale hingeless rotor, January 1994, American Helicopter Society Aeromechanics Specialist Conference, San Francisco, CA, USA.
49. DRELA, M. XFOIL: *An Analysis and Design System for Low Reynolds Number Airfoils, Low Reynolds Number Aerodynamics*, MUELLER, T. (Ed), *Lecture Notes in Engineering*, 1989, **54** pp 1-12, Springer Berlin, Heidelberg, Germany.

https://doi.org/10.1017/S0001924000010496 Published online by Cambridge University Press